Calibration Methods for Charge Integrating Detectors

D. Mezza[*,a], J. Becker[b], L. Carraresi[c,d], A. Castoldi[e,f], R. Dinapoli[a], P. Goettlicher[g], H. Graafsma[g,h], D. Greiffenberg[a], H. Hirsemann[g], A. Klujev[g], M. Kuhn[g], S. Lange[g], T. Laurus[g], S. Maffessanti[g], A. Marras[g], A. Mozzanica[a], J. Poehlsen[g], S. Redford[a], C. Ruder[a], B. Schmitt[a], I. Sheviakov[g], X. Shi[a], U. Trunk[g], S. Vetter[a], J. Zhang[a], M. Zimmer[g]

[a] *Paul-Scherrer-Institut (PSI), Forschungsstr. 111, 5232 Villigen, Switzerland*
[b] *X-Spectrum GmbH, Notkestr. 85, 22607 Hamburg, Germany*
[c] *Università degli studi di Firenze, Via B. Rossi 1, 50019 Sesto Fiorentino, Italy*
[d] *INFN Firenze, Via B. Rossi 1, 50019 Sesto Fiorentino, Italy*
[e] *Politecnico di Milano, P.za L. da Vinci 32, 20133 Milano, Italy*
[f] *INFN Milano, Via G. Celoria 16, 20133 Milano, Italy*
[g] *Deutsches Elektronensynchrotron DESY, Notkestr. 85, 22607 Hamburg, Germany*
[h] *Mid Sweden University, Holmgatan, 852 30 Sundsvall, Sweden*

Abstract

Since the introduction of the extremely intense X-ray free electron lasers, the need for low noise, high dynamic range and potentially fast charge integrating detectors has increased significantly. Among all the problems that research and development groups have to face in the development of such detectors, their calibration represents one of the most challenging and the collaboration between the detector development and user groups is of fundamental importance. The main challenge is to develop a calibration suite that is capable to test the detector over a wide dynamic range, with a high granularity and a very high linearity, together with a certain radiation tolerance and the possibility to well define the timings and the synchronization with the detector. Practical considerations have also to be made like the possibility to calibrate the detector in a reasonable time, the availability of the calibration source at the experimental place and so on. Such a calibration test suite is often not represented by a single source but by several sources that can cover different parts of the dynamic range and that need to be cross calibrated to have a final calibration curve. In this respect an essential part of the calibration is also to develop a mathematical model that allows calibrating the entire dynamic range, taking into account features that

[*] Corresponding author, email: davide.mezza@psi.ch

are calibration source and/or detector specific. The aim of this contribution is to compare the calibration for the AGIPD detector using several calibration sources such as internal current source, backside pulsing, IR pulsed laser, LED light and mono-energetic protons. The mathematical procedure used to calibrate the different sources will be discussed in great detail showing how to take into account a few shortcomings (like pixel coupling) that are common for many charge integrating detectors. This work has been carried out in the frame of the AGIPD project for the European X-ray Free Electron Laser.

Key words: 2D Detector; Instrumentation for FEL; X-Ray Detectors; Hybrid pixel detector; Detector calibration.

---

1. Introduction

In this contribution a mathematical model for the calibration of a charge integrating detector will be developed and the comparison between several calibration sources will be shown. The detector that has been used for the case study is the AGIPD (Adaptive Gain Integrating Pixel Detector) [1][2] detector developed for the European X-ray Free Electron Laser (EuXFEL) [3]. Different calibration sources and their combination for the calibration of large-format X-ray imagers for the EuXFEL over a wide range has been discussed also in [4].

The EuXFEL operates with pulse trains at a fundamental repetition frequency of 10 Hz. Each pulse train consists of up to 2700 X-ray photon pulses with a temporal separation of 222 ns, corresponding to a frame rate of 4.5 MHz (total pulse train duration 600 μs). Each photon pulse has a duration of < 100 fs (rms) and contains up to 10^{12} photons in an energy range between 250 eV and 25 keV. On one hand, these singular and innovative features open the way to new scientific opportunities, but on the other hand set extreme challenges for the development of the detectors [5]. AGIPD is a 2D hybrid pixel detector system developed to fulfill the requirements of this XFEL. To cope with the large dynamic range (from now on DR) the first stage of the ASIC is a charge sensitive preamplifier with three different gains that are dynamically switched by means of a comparator [6]. To provide the same data quality as a single photon counter and to be limited by the statistics, the noise of the detector has to be below the Poisson limit over the entire DR. This was confirmed by measurements. To cope with the 4.5 MHz pulse rate an intermediate in-pixel memory is needed and is realized with two analog storage cell matrices (one to store the information of the pulse height and one to store the information of the gain) of 352 storage cells occupying around 80% of the pixel area (200 x 200 μm^2). Another consequence of the high speed, as will be shown and explained in the next sections, is that the open-loop low frequency gain of the preamplifier is limited (average value < 15) and therefore a not negligible coupling between the pixels is present.

Due to all the features just mentioned, AGIPD represents the perfect test case to try, compare and assess different calibration methods and find advantages and weak spots of the different techniques.

The first aim of this contribution is to develop a mathematical model for the calibration of the DR of this detector. This will be done in two steps: first, develop an ideal case model and in a second phase implement a correction to take into account the coupling between the pixels that is critical for this detector. After that compare different calibration methods and sources in terms of the aspects listed above. All the measurements shown in this paper are acquired on the same pixel and the same storage cell, at the same temperature (20 °C), gain (standard gain mode, explained later) and the same sensor bias voltage of 240 V. The version 1.1 of the AGIPD ASIC [7] was used.

The calibration method used for the AGIPD detector is explained in [8].

This paper is organized as follows:

- Sec. 2: general explanation of the working principle of the AGIPD ASIC;
- Sec. 3: ideal case calibration;
- Sec. 4: absolute calibration in the HG region by means of fluorescence photons;
- Sec. 5: capacitive coupling between pixels;

- Sec. 6: source properties;
- Sec. 7: general overview of the calibration sources;
- Sec. 8: DR scan with the internal current source;
- Sec. 9: DR scan with an LED light;
- Sec. 10: DR scan pulsing the backside of the sensor;
- Sec. 11: DR scan with an IR pulsed laser;
- Sec. 12: DR scan with a pulsed monoenergetic proton beam;
- Sec. 13: offset obtained by triggering the gain switching without signal.
- Sec. 14: comparison of results.

A summary will follow in Sec. 15.

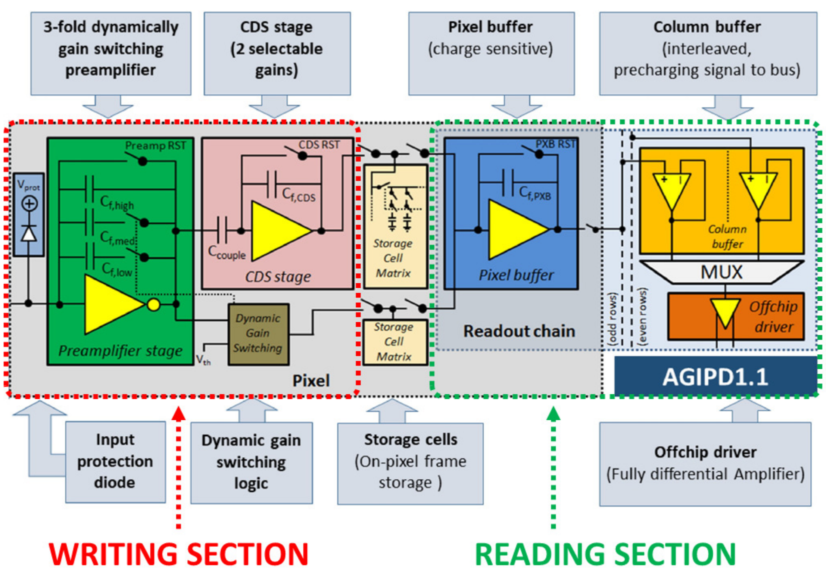

Figure 1: AGIPD scheme and working principle. The writing and reading sections are highlighted.

2. AGIPD working principle

The working principle of the AGIPD ASIC has been explained in [2], however, the “writing section” (see Fig. 1), from the input to the storage cell, is explained here in more detail since the calibration depends entirely upon its working principle. The “readout section” (from the pixel buffer to the output of the ASIC) has a gain that does not depend on the incident radiation and therefore constitutes only a constant scaling factor in the calibration process. For the rest of this paper we will refer to the entire on-chip readout chain, from the input of the preamplifier to the output of the fully differential offchip driver, as the analog readout chain.

The first stage of the amplification chain is a charge sensitive preamplifier with three different gains that are dynamically switched, depending on the number of incoming photons, by means of a comparator. The working principle is shown in Fig. 2.

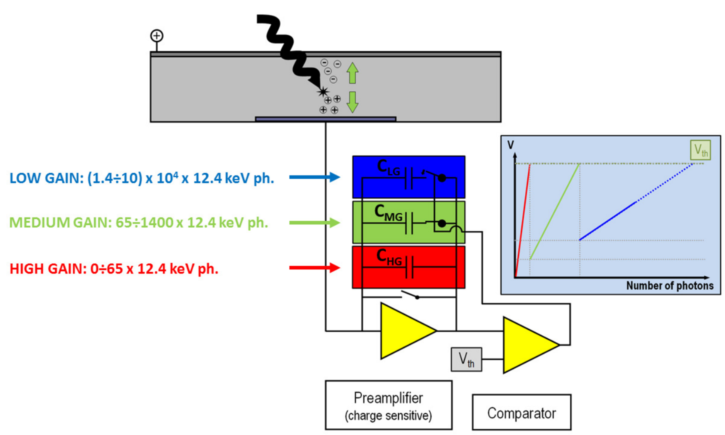

Figure 2: Working principle of the preamplifier and the comparator. The three gain regions (high, medium and low) are visible. The number of photons indicating the three different regions are arbitrary since the switching threshold can be adjusted and there might be also variation in several parameters (offset, gain etc.) from pixel to pixel.

At the beginning of the acquisition, only a small capacitor is connected in the feedback loop of the preamplifier, resulting in the maximum sensitivity (gain) which is proportional to $\frac{1}{C_{fb}}$. In the ideal case (preamplifier with infinite open loop gain) a gain in terms of output voltage as a function of the energy released by the photons impinging on the considered pixel can be expressed in the form:

$$G_{pre}[\frac{V}{eV}] = \frac{V_{out,pre}}{E_{ph}} = \frac{q}{\epsilon \cdot C_{fb}} \quad (1)$$

Where ϵ represents the mean energy for the $e^- - h^+$ creation (3.62 eV/couple in Si) and q the elementary charge. The first gain is called high gain (HG) and $C_{fb} = C_{HG}$. In this region, the noise is the lowest and it has an average value of 320 e^- rms, which allows having single photon resolution at 12.4 keV with a signal to noise ratio of around 11. When the number of incoming photons further increases and the level of the output of the preamplifier reaches the threshold of the comparator the first gain switching occurs. The gain switching is obtained by adding a capacitor in parallel to the first feedback capacitor ($C_{fb} = C_{HG} + C_{MG}$) obtaining a lower gain at the price of higher noise. In the second gain region, called medium gain (MG) region, the sensitivity is reduced and the single photon resolution (at the target energy of 12.4 keV) is lost but it is possible to reach a higher dynamic range without running into the saturation of the preamplifier. However, if the number of photons further increases at the level that the comparator threshold is reached again a second gain switching occurs adding a second capacitor in parallel to the first two and resulting in a third gain region, called low gain (LG) region where $C_{fb} = C_{HG} + C_{MG} + C_{LG}$. In this region the sensitivity is minimum and the dynamic range and the noise are maximum. The mechanism just described allows to have at the same time single photon resolution (at the target energy of 12.4 keV) in the HG region and reach almost up to 10^4 x 12.4 keV photons in the LG region. The preamplifier is followed by a correlated double sampling (CDS) stage that allows to remove the reset noise of the preamplifier and provide an additional gain factor. The user can select between standard gain mode (maximum DR, the one chosen in this contribution) or high gain mode (less noise) of the CDS and this will not change during the acquisition.

Fig. 3 describes the full writing cycle highlighting the main timings. In the

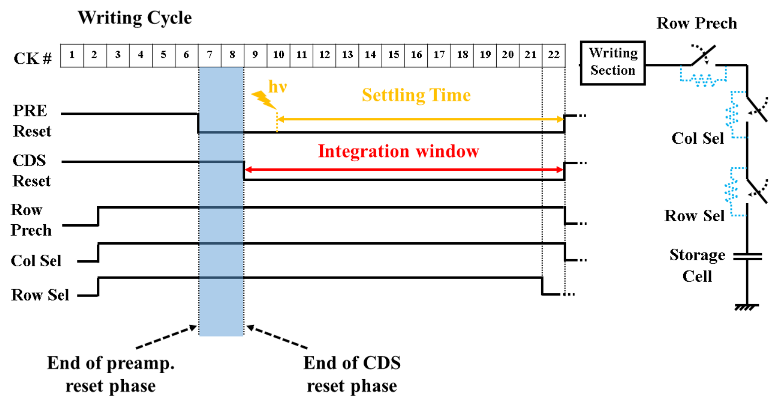

Figure 3: Writing cycle timings. In the real case the clock frequency is 100 MHz (1ck = 10 ns). The integration window and the settling time are highlighted, as well as the reset phase of the preamplifier and the CDS stage. In light blue the time between the two reset phases. On the right side there is a sketch of the writing section and a single memory cell, with the three access switches. In dotted light blue are the ON resistances of the switches.

real case, the clock frequency is around 100 MHz (1ck = 10 ns). Before the acquisition of every single image, the preamplifier needs to be reset for 60 ns to completely remove the charge on the feedback capacitor. The CDS stage is kept in reset for 20 ns longer than the preamplifier to remove the reset noise of the preamplifier. Therefore there will be 20 ns in between the two reset phases where the preamplifier is active and the CDS stage is still in reset. The effect of photons arriving during this phase on the calibration will be discussed is Sec. 9. There are three switches to access every single storage cell, each one with its own ON resistance, therefore a certain time is required to sample the full signal into the storage cells. The time between the release of the reset of the CDS and the disconnection of the storage cell (by means of the last switch) is called integration window and in the real case, this is 130/140 ns. The time between the arrival of the signal (radiation or electrical stimulus) and the disconnection of the storage cell is called settling time. The settling time is the time the writing section has to amplify the signal and write it into the storage cell. The time to write the signal into the storage cell is not negligible due to the finite

ON resistance of the access switches. The results of a too short settling time were shown in [2] and will also be briefly discussed in Sec. 9.

To perform all the measurements that will be shown in this contribution, a single chip test readout system has been used. This system is different from the readout system used for the final detector at the EuXFEL, in particular, the maximum clock frequency of the test system is 80 MHz ($T_{ck,test} = 12.5$ ns). The clock frequency at which the AGIPD ASIC is running is half of the one of the test system or 40 MHz ($T_{ck,ASIC} = 25$ ns). Due to this fact, the EuXFEL timings cannot be perfectly reproduced with the test system. However, the ASIC was programmed in a way that the relevant timings (e.g. the minimum reset time of preamplifier and CDS, the integration time and the settling time) were respected. In particular, with the described test system it is possible to introduce a "wait-at" and a "wait-for" to "freeze" the writing cycle at a given point for a certain amount of clock cycles, in unit of the test system clock or 12.5 ns. In all the measurements the nominal integration time is 137.5 ns (if changed it is explicitly mentioned) and the settling time is 125 ns.

3. Ideal case calibration

Due to the working principle just explained above the calibration requires in the ideal case the determination of 6 parameters per pixel: 3 gains $m_{\#\#}$ and 3 offsets $q_{\#\#}$ (see equations (2), (3) and (4)).

$$y_{HG}[ADU] = m_{HG}[\frac{ADU}{keV}] \cdot x_{HG}[keV] + q_{HG}[ADU] \tag{2}$$

$$y_{MG}[ADU] = m_{MG}[\frac{ADU}{keV}] \cdot x_{MG}[keV] + q_{MG}[ADU] \tag{3}$$

$$y_{LG}[ADU] = m_{LG}[\frac{ADU}{keV}] \cdot x_{LG}[keV] + q_{LG}[ADU] \tag{4}$$

Where x_{HG}, x_{MG} and x_{LG} are the portions of the x-axis belonging to the HG, MG and LG regions respectively.

Due to the storage cell to storage cell variation another 2 parameters per storage cell are required for the readout section. One to factorize the gains and one for the offsets. Note that for practical use of the detector these equations have to be inverted to determine the total energy (or number of photons) from ADU and the used gain.

In order to have as few parameters as possible to represent the calibration curve, the linearity of the measured system output curve is important. The measured linearity of the output curve can be affected by several factors:

- Linearity of the analog readout chain;
- Linearity and granularity of the calibration source;
- The parameter used to scan the DR.

The first one is obvious since the output of the ASIC can be mathematically seen as the convolution between the input signal and the pulse response of the analog readout chain and therefore, any non-linearities in the analog readout chain are reflected in the measured system output curve. The same is true for the non-linearities of the calibration source (second point) however here a more detailed discussion is needed and will be done in Sec. 7. The last point concerns the way the measurement is done, i.e. which parameter is used to scan the DR and how this can influence the linearity of the output. As will be shown in Sec. 8 and 9, one of the parameters that can be used to scan the DR is the integration time. In this case, if any reference (voltages or currents on the ASIC) are changing in time this might reflect as a non-linearity of the output curve even if this is not strictly related (or not only) to the analog readout chain or the calibration source.

4. Absolute gain calibration in HG region: fluorescence photons

The best and easiest way to obtain an absolute calibration in the HG region in terms of a conversion factor $m_{ph}[\frac{ADU}{keV}]$ is to irradiate the detector with fluorescence photons of possibly different energies and fit the main emission peaks. In Fig. 4 and 5 the spectra acquired with Mo and In fluorescence photons are shown. The noise peak (black), three Mo and two In peaks respectively were fitted and a conversion factor $m_{ph} = (12.455 \pm 0.007) \frac{[ADU]}{[keV]}$ was obtained.

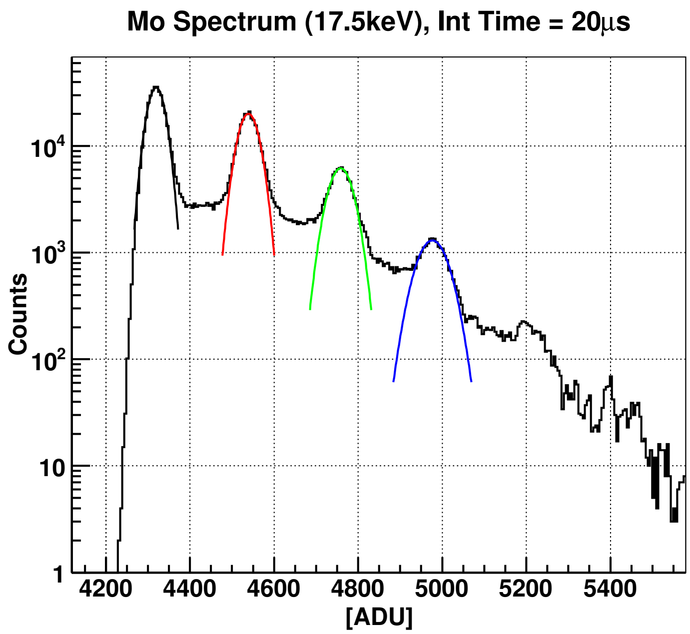

Figure 4: Spectrum acquired with Molybdenum (17.5 keV) fluorescence photons on one pixel. Three peaks are fitted to extract the absolute calibration factor in the HG region.

Fluorescence photons are essential to provide an absolute calibration factor in the HG region however even with higher photon energies and more photon peaks it is not possible to explore more than the initial part of the HG (in this case 52.5 keV). Furthermore, the noise in the MG and LG does not allow single photon resolution, therefore, to calibrate the detector one has to use other means for the lower gains.

One of the problems of the calibration is the coupling between pixels. This problem was shown in [11] and is also present in the AGIPD detector.

5. Pixel to pixel coupling

From now on we will refer to the pixel under test as central (CE) pixel and to the pixels around the central pixel as the neighboring pixels as in Fig. 6. When

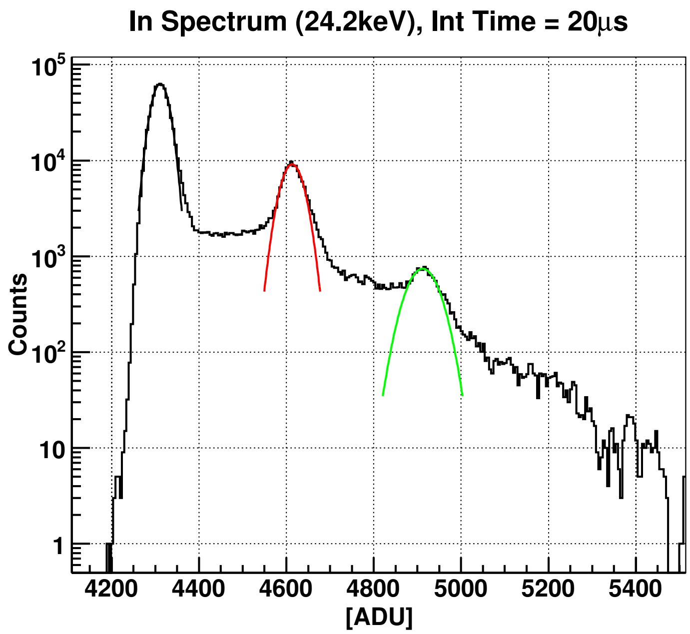

Figure 5: Spectrum acquired with Indium (24.2 keV) fluorescence photons on one pixel. Two peaks are fitted to extract the absolute calibration factor in the HG region.

a certain amount of charge is generated in the sensor by the incident radiation, even if this is entirely collected by the CE pixel (no charge sharing effect), the virtual ground potential changes due to the low dc gain of the preamplifier, inducing a signal in the neighboring channels through the coupling capacitors. This charge signal is taken away from the central channel. The coupling has been modelled in various ways in strip detectors [12][13][14]. In hybrid detectors also parasitic capacitances of the connections between the ASIC and sensor or on the ASIC have to be taken into account. However, in the case of AGIPD these are negligible.

To explain the capacitive coupling we use a simplified model with three pixels. We will refer to Fig. 7 where:

- Q_{tot} is the total charge generated in the sensor by the incident radiation;

- Q_i, Q_{i+1} and Q_{i-1} are the charges collected by the central channel (i) and

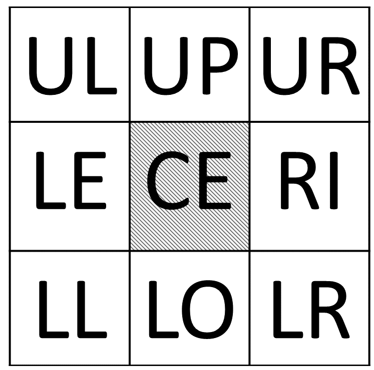

Figure 6: 3 x 3 pixel cluster considered. The central (CE) pixel is the one under test. The others are the eight neighbors. UL = upper left, UP = upper, UR = upper right, LE = left, RI = right, LL = lower left, LO = lower, LR = lower right.

the two neighbors (i+1 and i-1);

- C_{back} is the coupling of a pixel with the backside of the sensor assumed to be the same for the three pixels;

- $C_{coup,i+1}$ and $C_{coup,i-1}$ are the coupling capacitances between the central pixel and the two neighbors. This capacitances can have small variations from pixel to pixel;

- G_i, G_{i+1} and G_{i-1} are the open-loop gains of the preamplifiers.

The coupling can be explained in 6 steps (indicated by the circled numbers in violet in Fig. 7):

1. The charge is generated in the sensor by the incoming radiation. The negative charges are collected at the backside while the positive ones are collected by the central channel (i);
2. The charge is integrated on the feedback capacitor of the preamplifier;
3. There will be an output voltage signal proportional to the collected charge;
4. Due to the finite gain G_i the input node of the preamplifier is not an ideal virtual ground therefore there will be a residual voltage error signal on the input of CE;

5. Because of the presence of the coupling capacitances between the different pixels, and the voltage at the input of CE, a charge is induced in the neighboring channels. Due to variations in the coupling capacitance the induced charge might be different for every pixel. Moreover the charge induced in the neighboring pixels is taken away from the central channel;
6. An output signal appears at the output of the neighboring pixels.

In this picture the voltage variation of the input node of the neighboring pixels due to the finite gain of their preamplifier has been neglected since this is a second order effect that produces a variation of less than 1%. We want to stress that this effect does not have to be confused with the charge sharing between the different channels. The coupling effect is in fact due to the change of the pixel potential at the input due to the low DC gain of the amplifier. Charge sharing however refers to the case when the charge generated by the photons is collected by several pixels due to different physical effects such as diffusion, Coulomb repulsion or simply photons impinging at the border between pixels. The coupling effect can be noticed in Fig. 8 and 9 where the 2D maps of the energy measured by the CE pixel with respect to the RI and the UL pixels are shown. It is clearly visible that in correspondence of the Mo photon peaks on the CE pixel a percentage is also measured by the RI pixel. This is due to the coupling explained before. For the UL pixel, this effect is reduced. In general, for the 4 pixels in the corner (UL, UR, LL, LR), this effect is reduced because the coupling capacitance is roughly a factor of 4 smaller with respect to the one of the pixels at the 4 sides (UP, LE, RI, LO). To properly calibrate the system we have to evaluate the real conversion factor that takes the coupling between the pixels into account. By not doing so one would not conserve the total charge (Q_{tot} in Fig. 7) and therefore the energy released in the sensor by the incoming radiation.

Referring to Fig. 8 and 9 the slope of the line connecting the centers of the distributions can be evaluated:

$$\frac{\Delta y_i}{\Delta x} = \frac{E_{neigh,i}}{E_{CE}} = \frac{Q_{neigh,i}}{Q_{CE}} = k_i \tag{5}$$

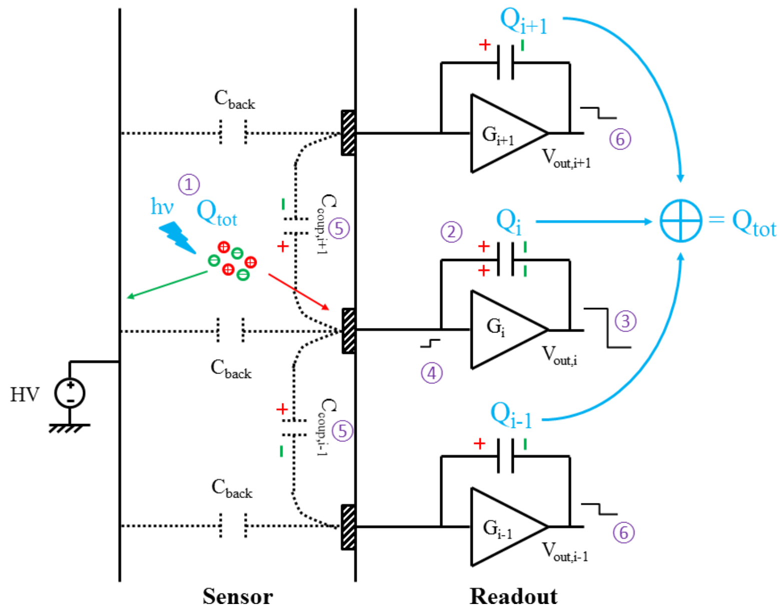

Figure 7: Scheme of the capacitive coupling between three pixels.

Where k_i is called coupling factor (of the CE pixel with the neighbor pixel i). The total energy can be expressed as:

$$E_{tot} = E_{CE} + E_{neigh,tot} = (1 + k_{tot}) \cdot E_{CE} \tag{6}$$

In (6) we have defined $E_{neigh,tot} = \sum_{i=1}^{8} E_{neigh,i}$ and $k_{tot} = \sum_{i=1}^{8} k_i$ as the total energy collected by the eight neighboring pixels and the total coupling factor of CE to these pixels. We can define a fractional charge c as the fraction of the energy (charge) going into the neighboring pixels with respect to the total energy released (generated charge):

$$c = \frac{E_{neigh,tot}}{E_{tot}} = \frac{E_{neigh,tot}}{E_{neigh,tot} + E_{CE}} = \frac{k_{tot}}{1 + k_{tot}} \tag{7}$$

The total coupling k_{tot}, in the HG for the CE pixel is 0.118 $\pm$ 0.003 (or 11.8% with an uncertainty of 3%) and apart from the border pixels, it is not changing significantly over the entire chip. The main source of variation comes from the electrical parameters (such as transconductance and threshold) of the input transistors that directly affect the DC gain of the preamplifier. The frac-

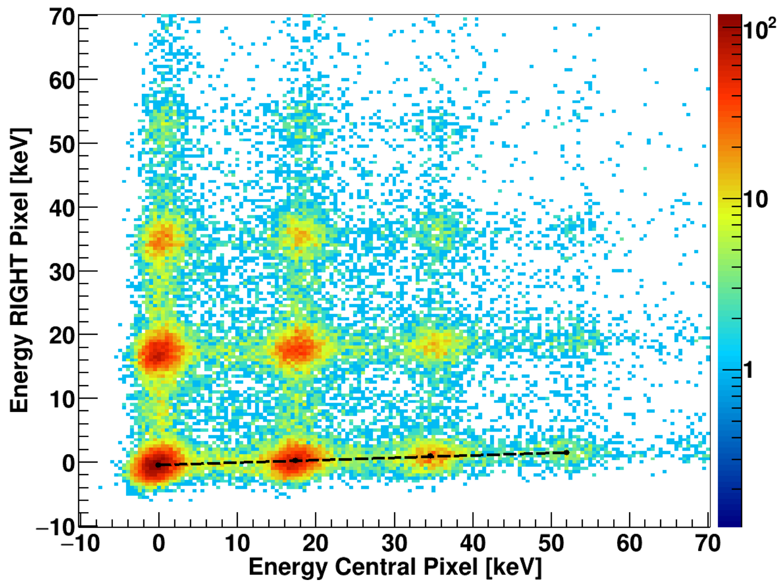

Figure 8: 2D map of the energy measured by the RI pixel vs CE pixel. Clearly visible is the slope of the line (dotted black) connecting the centers of the distributions in correspondence of the single Mo (17.5 keV) peaks.

tional charge can be directly calculated from (7) and is 0.1056 $\pm$ 0.0026. The conversion factor m_{ph} measured for a given pixel (CE) in the way described in Sec. 4 is connected with the energy measured by that pixel E_{CE} and is for the CE pixel (12.455 $\pm$ 0.007) $\frac{[ADU]}{[keV]}$. The real conversion factor is connected with the total energy E_{tot} and from (6) and (5) we can obtain the real conversion factor:

$$m_{ph,real} = m_{ph} \cdot (1 + k_{tot}) = \frac{m_{ph}}{1 - c} \tag{8}$$

For the CE pixel, this has a value of (13.925 $\pm$ 0.041) $\frac{[ADU]}{[keV]}$.

6. Calibration source properties and impact on the detector calibration

There are important aspects to consider when comparing different calibration sources and the output curves (DR scan in our case) obtained with them:

1. Testable DR;

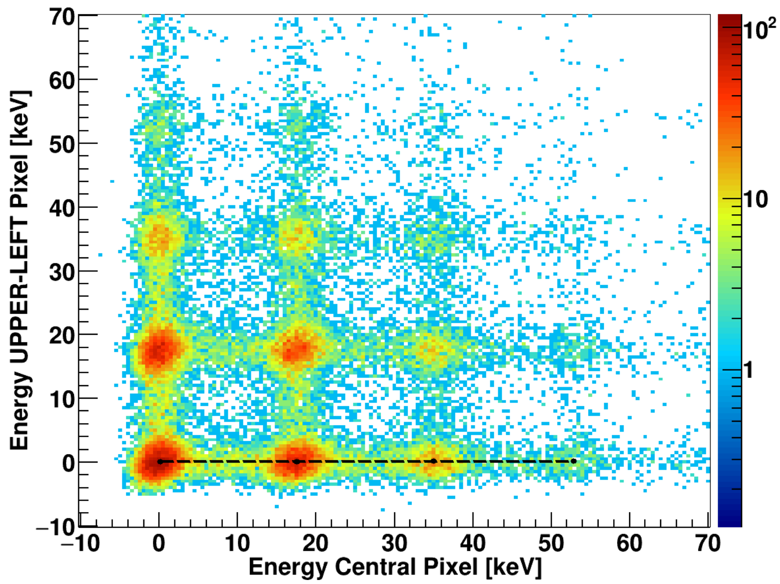

Figure 9: 2D map of the energy measured by the UL pixel vs CE pixel. The slope of the line (dotted black) connecting the centers of the distributions in correspondence of the single Mo (17.5 keV) peaks is almost negligible with respect to the RI pixel case.

2. Linearity of the calibration source;
3. Granularity (capability to finely test the DR);
4. Verifiability, meaning that the source performance can be verified independently from the detector;
5. Stability (in amplitude and/or time);
6. Time for calibration (how much detector area can be tested in a certain amount of time);
7. Availability "in-situ" (at the experimental site);
8. Synchronization (e.g. trigger to define the timings with respect to the detector);
9. Radiation tolerance (of the source).

Above mentioned are all the critical points that one should consider when choosing the calibration source. In the rest of this contribution we will mention only the critical points for the specific sources. The points 2) and 3) need a more in depth discussion.

The linearity of the calibration source is essential to measure the output curve and calibrate it. In some cases it is not possible, e.g. for the on-chip sources, to independently measure the linearity of the calibration source. Therefore it is very important to use different calibration sources to verify the calibration and to understand where the non-linearities are coming from, i.e. if they arise from the calibration source, the analog acquisition chain or from the way the measurement is performed (e.g. varying the integration time).

Another important aspect about the “quality” of a calibration source is its granularity, i.e. the capability of the calibration source to finely sample the DR. A source that is very linear but has a coarse granularity can only sample the DR with few points and in turn the non-linearity of the output curve might be overseen. Therefore, a figure of merit given in the next sections will contain the granularity of the source for a uniform sampling and/or the last and the first point before and after the gain switching to give a quantitative idea of how well the critical areas for this detector are sampled. These numbers will be given in addition to the linearity of the output curve in terms of maximum positive and negative deviations (in number of 12.4 keV photons) in the fitted range (all these results are collected in the summary Table 19).

7. General overview of the calibration sources

The sources that have been used and compared to calibrate the DR are:

1. X-ray photons;
2. Internal current source;
3. LED light;
4. Internal pulsed capacitor;
5. Sensor backside pulsing;
6. IR pulsed laser;
7. Pulsed monoenergetic proton beam.

The internal pulsed capacitor are not used here, the measurement results can be found in [8].

In the list above the first five sources are in principle usable to calibrate the full detector system while the last two are not. This is mainly due to the non-availability of this sources in-situ (i.e., at the experimental place) and the limited number of pixels that can be probed per unit of time. Therefore, these two sources were used only for comparison to and verification of the other calibration sources. These two sources were chosen because of their capability to simulate a high level of charge injection in the sensor, comparable to the one of the EuXFEL. This allows to test the pixel response under XFEL like conditions when a beamtime at the EuXFEL is not available. Moreover, both these sources are pulsed, providing a perfect synchronization with the detector readout timings.

The internal current source and pulsed capacitor are directly on-chip and they are usually extremely flexible due to the fact that they are fully programmable. Due to these advantages they are the perfect candidates to calibrate the full detector system. The main disadvantage is that the parameter used to scan the DR is the integration time, making the current source sensitive to offset drifts that are integration time dependent. The main disadvantages of the on-chip pulsed capacitor (see [8]) is the limited DR that can be probed and the relatively high non-linearity. Another important aspect to keep in mind (specifically for the on-chip calibration sources) is that there might be an offset due to switching the source on that has to be taken into account to have a common starting point for the calibration of all the sources. Moreover, the on-chip sources cannot be tested separately to assess their performance and they might be very sensitive to radiation damage.

The LED light has been chosen as a potential calibration source thanks to its capability to uniformly irradiate a vast area of the detector and its time stability. As for the current source, the parameter used to scan the DR is the integration time, therefore, the same problems as for the current source are present also for this source. The two main disadvantages are its asynchronicity (i.e., no trigger) and the need to remove the Aluminum from the backside of the sensor leaving the detector sensitive to (visible and IR) light.

The sensor backside pulsing was a solution proposed in [16] that is, in terms of the working principle, very similar to the on-chip pulsed capacitor with the only difference being that the pulsing capacitor is the sensor itself. This technique showed many advantages such as the very high linearity, the independence from the ASIC and the use of the sensor capacitance that is intrinsically highly radiation tolerant. The main disadvantages are the limited DR that can be probed and the simultaneous injection in all the pixels.

8. DR scan with internal current source

One of the possibilities to scan the DR is to use an on-chip current source to inject a constant current into the input (virtual ground) of the preamplifier. By changing the integration time, the charge injected increases proportionally and therefore it is possible to explore the entire DR.

On the AGIPD ASIC a current source per pixel has been implemented. It is fully programmable both in strength and timings (switch on/off). Moreover, also the pattern in which pixel a current is injected can be modified. Concerning the injection circuitry, the 64 x 64 pixels of the ASIC are divided into 64 sub-matrices of 8 x 8 pixels each (see Fig. 10). All sub-matrices are repeated over the entire ASIC, i.e. all sub-matrices are identical. The current source can be activated by means of a logical AND between two signals (TIROWM and TICOLM) obtaining an injection in a single pixel (total of 64 pixels on the entire ASIC) or single/multiple rows/columns, up to the entire chip. This feature makes the current source very flexible on one hand. However, because of the inter pixel coupling, an injection pattern dependent calibration of the output curve is needed.

The scan of the DR using the current source has been done for different injection patterns, changing the integration time. The calibration concept and the results will be shown for the two extreme cases of 64 and 4096 pixel injection

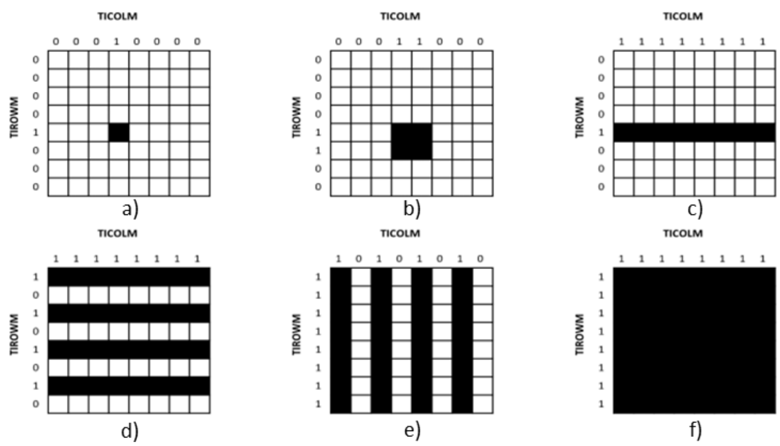

Figure 10: Possible programmable injection patterns that can be used to inject the current source in different number of pixels. The injection patterns are shown for a 8 × 8 pixels sub-matrix and can be chosen by means of programmable 2 × 8 bits programmable signals (TICOLM and TIROWM). The number of pixels injected per ASIC are: a) 64, b) 256, c) 512, d,e) 2048 and f) 4096.

(patterns a) and f) of Fig. 10). These two patterns correspond to the single pixel injection (CE injected and 0 neighbors) and injection in the entire ASIC (CE and all its 8 neighbors injected). It is worth to mention that, since the current source requires power from the ASIC, in case of a high intensity setting and many current sources switched on, this might generate a power drop across the chip that can not only affect the calibration but might also cause changes in the chip behaviour with respect to operation without current sources (e.g. the DR can result to be different). For the specific ASIC described in this paper, to properly scan the HG region (have enough points given the granularity of the clock) the current injected is in the order of a few tens of nA, resulting in a power consumption that is negligible with respect to the total power consumption.

The DR was scanned by changing the integration time in steps and changing the integration time step three times as shown in Table 1 for the 4096 pixels injection case. In the first column of Table 1 the integration time steps are given in number of 80 MHz clock cycles. As can be seen there is a start and stop point, and a delta (Δ) that is the granularity in number of clock cycles to sample the interval between start and stop. This is the integration time that is used to integrate the current injected by the current source into the virtual ground of the preamplifier. This time has to be added to the 137.5 ns integration time that is used as default value. The step size is then reported in ns in the second column and in number of 12.4 keV photons in the third column (number calculated by using the procedure shown in Sec. 8.1). The reason for different integration time steps is to finely sample the HG region, and in particular, the area after the first gain switching and then sampling the MG and LG regions with more coarse steps to reduce the measurement time. Despite the coarse steps, the MG and LG regions result to be well sampled (in terms of number of points) since the gain is lower. The best achievable granularity for our system (with the clock frequency of 80 MHz, 1 ck = 12.5 ns) and the minimum current intensity is around 1.5 x 12.4 keV photons.

Table 1: Integration time steps used for the current source injection

(Start : Δ : Stop) [# CK]	Δ [ns]	Δ [x 12.4 keV ph.]
(4 : 2 : 82)	25	3.05
(84 : 50 : 2184)	625	76.3
(2234 : 160 : 10234)	2000	244

A relevant problem with the current source switched off is the variation of the offset with the integration time. The red curve of Fig. 11 shows the offset variation, measured in the HG region, as a function of the integration time. As can be seen, this variation is highly non-linear (maximum variation around 300 ADU) and, if not corrected, it produces a strong non-linear output leading to a wrong estimation of the offset and the gain. To correct this effect, for every single acquisition time the variation of the offset has to be subtracted. In doing so, one has to be careful that the offset variation has to be acquired in the same gain region (HG, MG or LG) as the point that we want to correct. To clarify one can imagine that if the offset variation is due to a drift of a reference voltage after the preamplifier then the offset variation is independent from the gain region we are in. If for example, the offset variation is due to the leakage

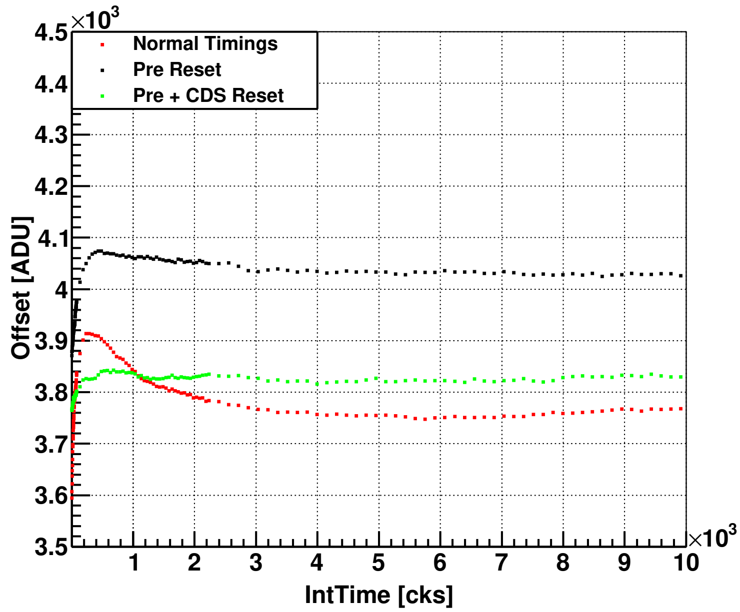

Figure 11: Offset variation in the HG as a function of the integration time for normal operation mode (red), with preamplifier in reset (black) and with both preamplifier and CDS stage in reset (green).

current of the input transistors of the preamplifier or the sensor or a shift of the virtual ground then the offset variation will depend on which working region we are in. This correction is very time consuming since every single pixel switches at a different time so the offset has to be acquired in the correct working region for every single pixel. From the measurement shown in Fig. 11 where the offset was measured as a function of the integration time keeping the preamplifier and then the CDS stage in reset, it is evident that the offset variation is due to drifts both before and after the preamplifier therefore a gain region dependent offset has to be acquired.

8.1. Calibration

As already mentioned in Sec. 8 the calibration of the data acquired with the current source is dependent on the injection pattern used. In Fig. 12 the effect of the inter pixel coupling is well visible. All the curves are acquired on the same pixel, with the same current intensity, but with a different injection pattern on the chip. The curve with the highest slope (light blue squares) is acquired injecting the current source in all the 4096 pixels. In this case, part of the charge injected in the CE pixel is given to the neighboring pixels because of the coupling, however, the same charge is given back to the CE pixel by the neighboring pixels in which a current is also injected. Therefore, in this case there is no charge lost to the neighbors, neglecting the second order effect of the pixel to pixel non-uniformity of the current source. In the case of single pixel injection (the curve with the lowest slope), the charge lost to the neighbors by the CE pixel is not given back resulting in a lower slope. Another important assumption is that the current generated by the current source is always the same whether the injection is made in a single or more pixels. This assumption is reasonable due to what was stated about the current consumption in Sec. 8. The individual coupling factors between the CE pixel and each single neighbor has been determined in order to calculate the proper coupling factor to use in the different cases.

The further calibration procedure consists of the following steps:

1. Subtract the offset variation as a function of the integration time in HG;
2. Extrapolate a linear fit of the curve in the HG to the offset acquired with the minimum integration time;
3. x-axis (IntTime) correction (translation to move the origin to x=0);
4. x-axis calibration (scaling to map integration time to charge);
5. y-axis (Amplitude) correction (scaling to account for the charge loss to neighbors).

Since in the MG and LG region the feedback capacitors of the preamplifier are bigger the coupling in these two gain regions can be neglected. Therefore, the following procedure is only applied in the HG region. As already mentioned, step 1) provides a curve with better linearity. Performing this, the measurement

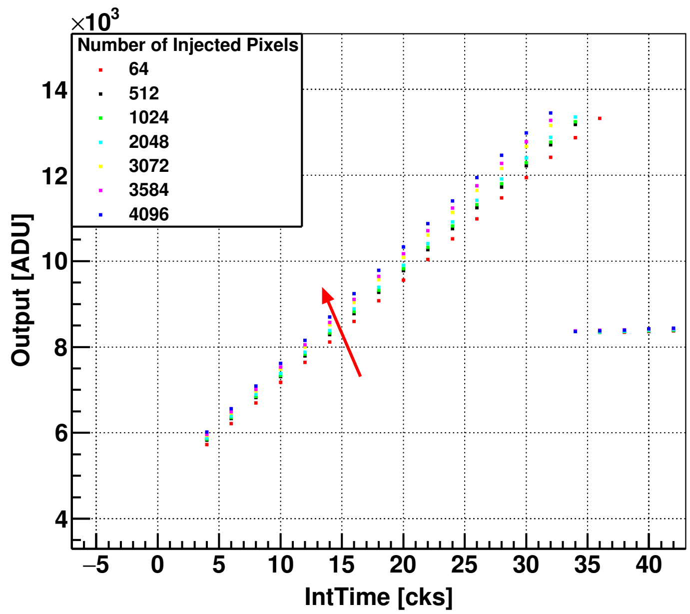

Figure 12: Zoom of the HG region of the DR scan obtained with the current source injection. The different curves are acquired on the same pixel but with a different injection pattern on the chip. The red arrow indicate the direction of increase of the number of injected pixels. The curve with the lowest slope (black squares) is acquired injecting the current source in one pixel every 64 while the highest one (light blue squares) is acquired injecting the current source in all the 4096 pixels. All the other curves are obtained injecting the current in 512, 1024, 2048, 3072 and 3584 pixels.

errors on offset and amplitude have to be considered to compute the measurement error of the new corrected amplitude. Step 2) consists of extrapolating the crossing point between the DR scan curve and the offset acquired with the minimum integration time that correspond to the output signal when no charge is injected, i.e. when the integration time is 0. Step 3) consists of correcting the x-axis by the difference of the crossing point and 0 such that:

$$x_{\#pix,new}\,[\#CK] \;=\; (x_{\#pix,old} \;-\; x_{cross,\#pix})\,[\#CK] \tag{9}$$

This step allows having a common 0 on the x-axis and takes into account the offset of the calibration source, which in the case of the current source is due to

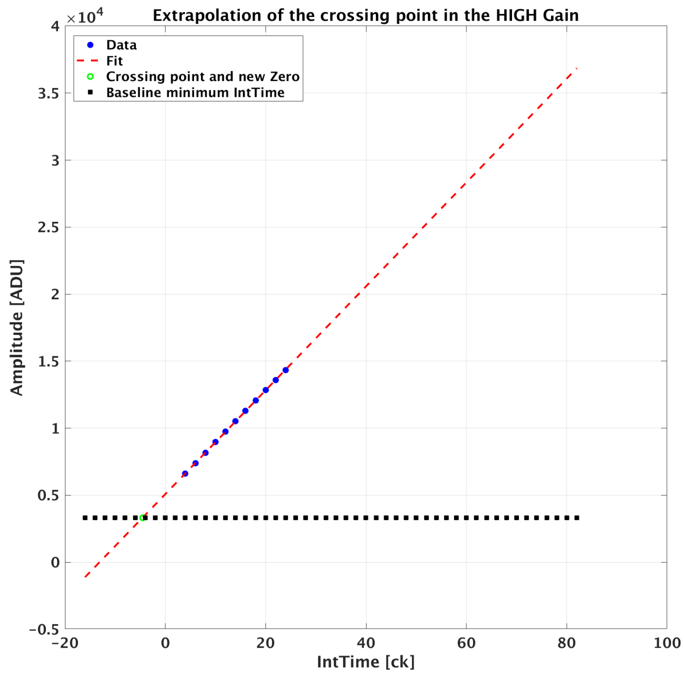

Figure 13: Extrapolation of the crossing point (green) between the offset acquired with the minimum integration time (black) and the HG scan (blue) for the CE pixel for 4096 pixel injection and after the offset variation subtraction.

the charge injected by switching the source on. In the two extreme cases this is:

$x_{cross,64pix} \;=\; (-6.345 \;\pm\; 0.006)\;[\#CK]$

$x_{cross,4096pix} \;=\; (-6.231 \;\pm\; 0.006)\;[\#CK]$

Step 4) consists of converting the x-axis from time to energy (keV or $N \times 12.4\, keV ph.$) and considering the curves in Fig. 12, in the HG region one can write:

$$y_{64}[ADU] \;=\; m_{64}[\frac{ADU}{\#CK}] \cdot x_{64,new}[\#CK] + q_{64}[ADU] \qquad (10)$$

$$y_{4096}[ADU] \;=\; m_{4096}[\frac{ADU}{\#CK}] \cdot x_{4096,new}[\#CK] + q_{4096}[ADU] \qquad (11)$$

For the equations (10) and (11):

$x_{64,new}[\#CK] \;=\; x_{4096,new}[\#CK]$

$y_{64}[ADU] \;\neq\; y_{4096}[ADU]$

$m_{64}[\frac{ADU}{\#CK}] \neq m_{4096}[\frac{ADU}{\#CK}]$

To calibrate the output curves obtained with the current source we can first assume that by making a linear fit of the curves the offset $q_{\#pix}$ can be measured and subtracted:

$$(y_{64} - q_{64})[ADU] = m_{64}[\frac{ADU}{\#CK}] \cdot x_{64,new}[\#CK] \tag{12}$$

$$(y_{4096} - q_{4096})[ADU] = m_{4096}[\frac{ADU}{\#CK}] \cdot x_{4096,new}[\#CK] \tag{13}$$

Moreover:

$$m_{64}[\frac{ADU}{\#CK}] \propto \frac{I_{nom} - I_{coup}}{C_{HG}} \tag{14}$$

$$m_{4096}[\frac{ADU}{\#CK}] \propto \frac{I_{nom}}{C_{HG}} \tag{15}$$

Where I_{nom} is the nominal current injected in the virtual ground of the preamplifier and I_{coup} is the current lost by the considered pixel due to the coupling and since $I \propto Q$ (the current is proportional to the charge):

$$I_{coup} = c_{\#pix} \cdot I_{nom} = c \cdot I_{nom} \tag{16}$$

Where $c_{\#pix}$ is the coupling factor that depends on the pattern of injection which in the considered case is c as defined in equation (5). From equations (14), (15) and (16):

$$m_{64} \propto \frac{I_{nom} \cdot (1-c)}{C_{HG}} = m_{4096} \cdot (1-c) \tag{17}$$

The equation (17) can be used to calibrate the x-axis:

$$x_{64}[keV] = \frac{m_{64}[\frac{ADU}{\#CK}]}{m_{ph}[\frac{ADU}{keV}]} \cdot x_{64,new}[\#CK] \tag{18}$$

$$x_{4096}[keV] = \frac{m_{4096}[\frac{ADU}{\#CK}]}{m_{ph,real}[\frac{ADU}{keV}]} \cdot x_{4096,new}[\#CK] \tag{19}$$

Where m_{ph} and $m_{ph,real}$ are defined as in the equation (8). Equations (18) and (19) represent the calibration of the x-axis since:

$$x_{64}[keV] = x_{4096}[keV] = x[keV] \tag{20}$$

From equations (18), (19) and taking into account the equation (20) one can correct the y-axis (that is the point 5) in the steps listed above) in the HG region and from equations (12) and (13) with few calculation:

$$y_{64,cal}\ [ADU] \ = \ [(y_{4096} \ - \ q_{4096}) \ \cdot \ (1 - c) + q_{64}]\ [ADU] \tag{21}$$

Equation (21) represents the new y-axis in the HG region when the current is injected in only 1 pixel per sub-matrix. When the current is injected in all the pixels no correction has to be applied to the y-axis.

In Fig. 14 the output curves (CE pixel) obtained for the same injection patterns of Fig. 12 and calibrated by just applying a simple calibration using the same correction factor m_{ph} for all the curves, i.e. neglecting the coupling between the pixels. By doing so all the curves are aligned in the HG region however the error on the slope and offset are propagated to the MG and LG.

The current source data have been calibrated with the procedure explained in this section and the results of gains (slopes), offsets and errors by linearly fitting the calibrated curves are reported in Tables 2 and 3. The calibrated output curve for the 4096 pixel injection pattern is shown in Fig. 15.

Table 2: Gains and offsets in MG

#Pix inj.	Gain $\frac{[ADU]}{[keV]}$	Offset $[ADU]$
64	0.3674 ± 0.0001	8071.6 ± 0.1
4096	0.3825 ± 0.0004	8110.8 ± 0.7

Table 3: Gains and offsets in LG

#Pix inj.	Gain $\frac{[ADU]}{[keV]}$	Offset $[ADU]$
64	0.07661 ± 0.00002	8462 ± 1
4096	0.0756 ± 0.0001	8574 ± 5

As can be seen, there is a difference of gains and offsets for the two different injection patterns that is not within the measurement error. This can be explained by looking at Fig. 16 and 17. In Fig. 16, the calibrated curves for the two extreme injection patterns (64 and 4096 pixels) in the MG region as well as

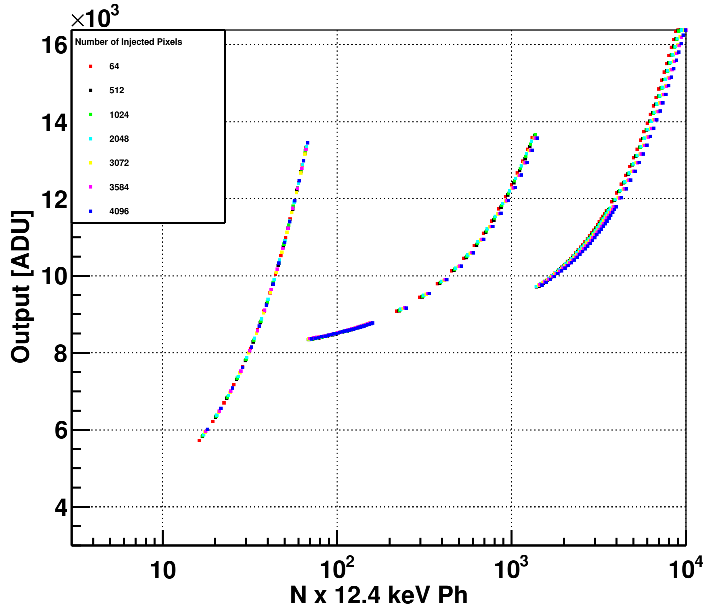

Figure 14: Output curves for the CE pixel for different injection patterns and calibrated using the same conversion factor m_{ph}, i.e. neglecting the coupling between the pixels. By definition the curves are aligned in the HG region however the error on the slope and the offset are then propagated to the MG and LG regions.

the linear fit (between 80 and 1200 x 12.4 keV ph.) are shown. As can be seen from Fig. 17, where the remainders of the fit are shown, there is a clear bending of the curve (non-linearity).

9. DR scan with an LED light

Another easy way to explore the DR is to illuminate the sensor with an intensity stable LED light, generating continuously in time charge in the sensor. This source is completely independent from the ASIC and therefore, it is radiation hard, does not require power from the ASIC and can be independently tested. To perform this measurement the Aluminum has to be removed from the backside of the sensor. This has been done on the prototype under test by chemical etching. Because of the removal of the Aluminum layer on the

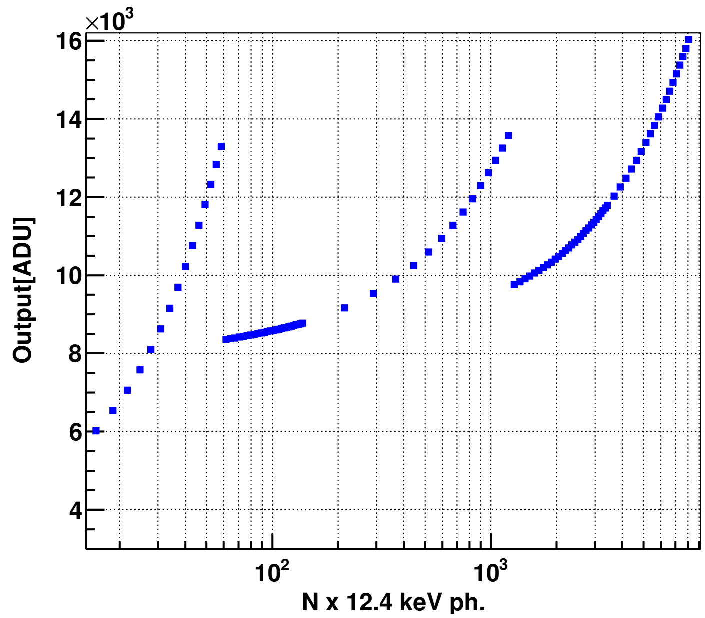

Figure 15: Calibrated output obtained using the on-chip current source. This curve is obtained with the 4096 pixel injection pattern.

backside of the sensor, the usage of this technique is very limited in practical applications.

The measurement was done in the same way as it was done for the on-chip current source. The integration time was changed as in Table 4. As can be noticed, the first two columns of Table 4 are identical to the ones of Table 1 while the third one is different. This is due to the intensity of the LED that is lower than the one of the current source, i.e. the charge injected per unit of time is a bit more than half of the one injected with the current source. This means that the granularity in this case is roughly 50% better and therefore the DR is more finely sampled. As for the current source this method is sensitive to a variation of the offset with the integration time.

The LED light is a continuous source so it is not synchronous with the AGIPD ASIC (no trigger signal is provided). Even if at a first glance this seems to be a disadvantage it makes this source very interesting and worth to be shown

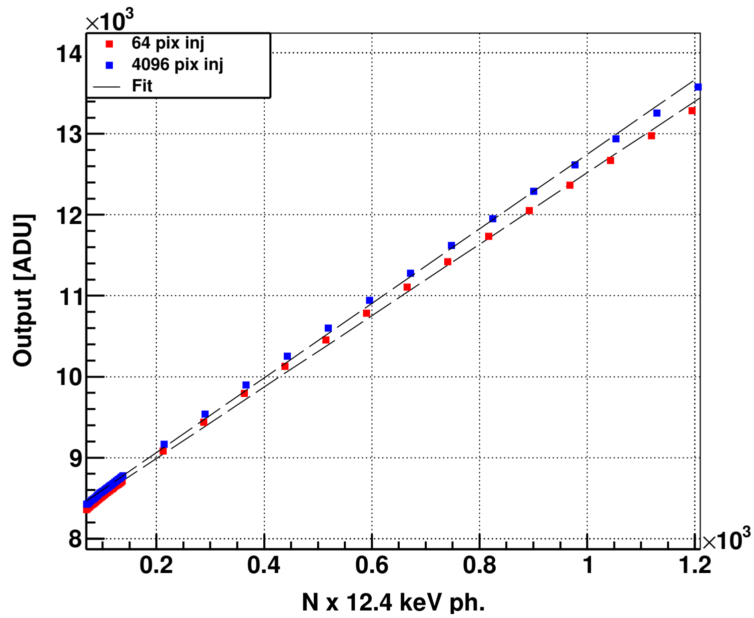

Figure 16: Calibrated output curve in the MG for the CE pixel for the two extreme injections schemes (64 pixels and 4096 pixels). In black the linear fit of the two curves. Fit limits (80,1200) x 12.4 keV ph.

Table 4: Integration time steps used for the LED light irradiation

(Start : Δ : Stop) [# CK]	Δ [ns]	Δ [x 12.4 keV ph.]
(4 : 2 : 82)	25	1.67
(84 : 50 : 2184)	625	41.5
(2234 : 160 : 10234)	2000	133.6

and discussed in this contribution because of its consequences:

1. The settling time (defined in Sec. 2) is by definition zero;
2. Charge injection is present between the reset phases of the preamplifier and the CDS (when the preamplifier is active and the CDS is still in reset).

The consequence of 1) is that the output of the CDS is sampled on the storage cell while this is still changing leading to a strong non-monotonicity of the response after gain switching (visible in the first few points, indicated

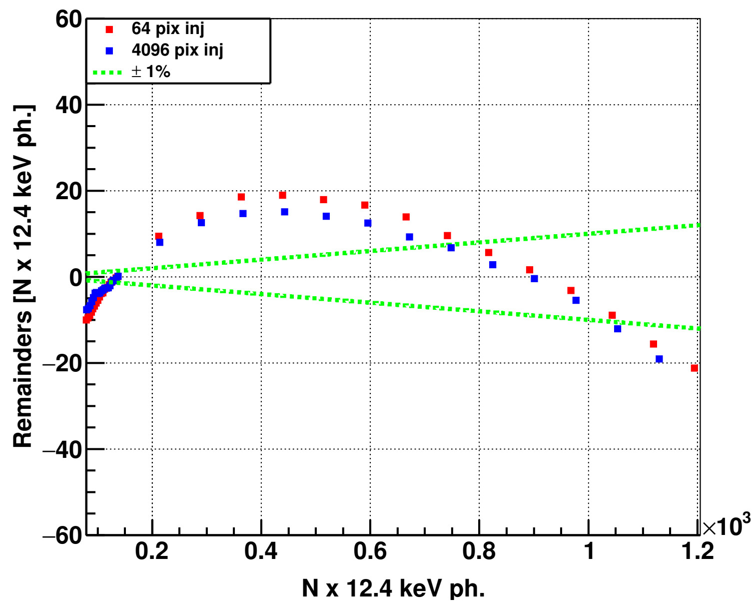

Figure 17: Remainders (in 12.4 keV ph.) obtained by subtracting the linear fit from the data of Fig. 16, in the fitted range. In green the ±1%.

with the red arrows, after the first gain switching in Fig. 18 and also discussed in [7]). It has to be mentioned that these points after the gain switching are also visible because of the fine granularity of this source. Since the gain switching is happening at the preamplifier level, the consequence of 2) is that the preamplifier switches gain at different signals of the CDS, causing an unknown offset in the MG and LG regions. This fact is particularly important since it might limit the use of this kind of detector with non-synchronous sources, e.g. synchrotrons.

9.1. Calibration

Since the scan parameter is the integration time the calibration of this source is the same as of the current source with the injection in 4096 pixels (the illumination is uniform in this case over the entire ASIC). The gains and offsets were extracted also in the case of the LED illumination keeping the same fit limits as for the current source. In Fig. 19 the MG range and the fit are shown and in

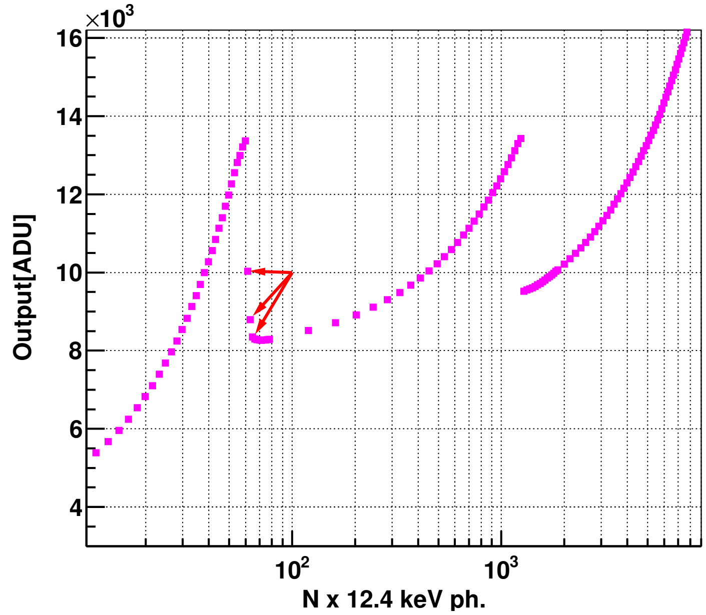

Figure 18: Calibrated output obtained irradiating the sensor with an LED. The red arrows indicate few points after the gain switching that causes a non-monotonicity of the curve. This is due to the fine granularity and the undefined timings, i.e. the settling time is zero.

Fig. 20 the remainders. As expected also in this case there is a visible bending of the curve. The fit results are reported in Table 5 and they differ from the one obtained with the current source more than the measurement error. The reason is, as already explained for the current source, the bending of the curve which is also slightly different from curve to curve. In addition, as explained in Sec. 9, the offset has also the unknown contribution of the charge integrated between the two reset phases of the preamplifier and the CDS.

Table 5: Gains and offsets for LED light

Gain region	Gain $\frac{[ADU]}{[keV]}$	Offset $[ADU]$
MG	0.3614 ± 0.0003	7996 ± 1
LG	0.0835 ± 0.0001	8153 ± 6

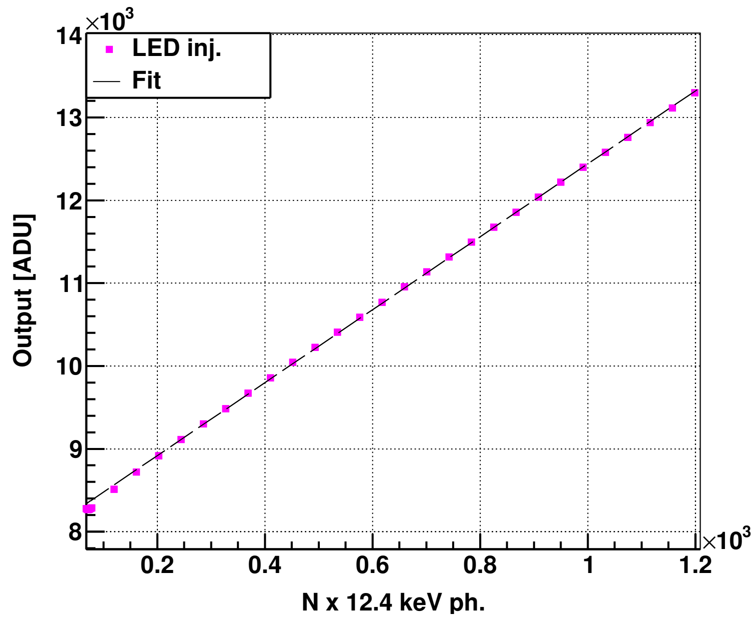

Figure 19: Calibrated output curve in the MG for the CE pixel for the LED illumination. In black the linear fit of the two curves. Fit limits (80,1200) x 12.4 keV ph.

10. DR scan with sensor backside pulsing

This technique has already been shown in [16] and used in [17]. It consists of AC-coupling a pulse generator to the backside of the sensor and to apply a voltage step of increasing amplitudes. In our case, a discrete components high voltage amplifier has been designed to amplify the voltage step from a waveform generator to provide an amplitude up to 35 V to the sensor. A trigger signal is provided by the waveform generator. The rising edge of the pulse has to be in the integration window, a settling time before the storage cell disconnection, and the falling edge of the pulse has to be outside this integration window, i.e. after the storage cell disconnection. Moreover, the pulse amplitude (in V) is limited by the high voltage applied to the sensor in order to avoid the forward bias of the sensor when the falling edge of the pulse occurs.

The sampling variable is reported in Table 6. The authors would like to

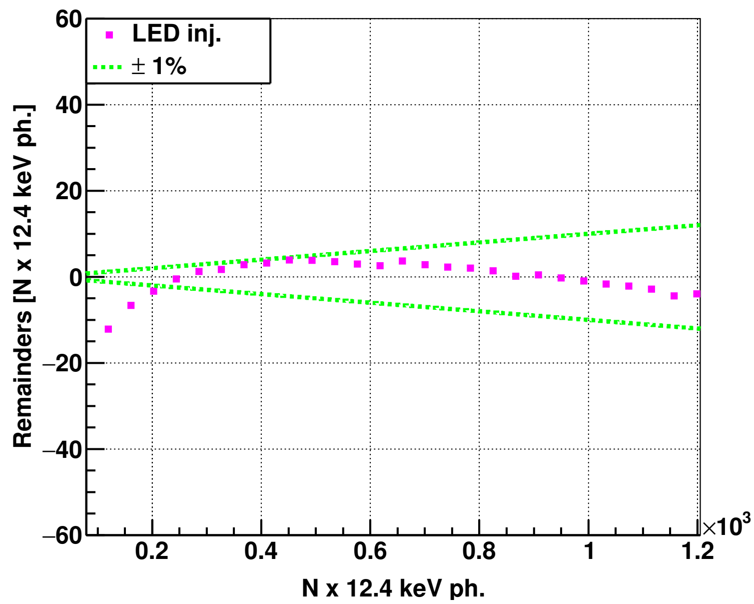

Figure 20: Remainders (in 12.4 keV ph.) obtained by subtract the linear fit from the data of Fig. 19, in the fitted range. In green the ±1%.

mention that the last point acquired in the HG region has been discarded, which is the reason of the apparent discrepancy between the granularity of 1.95 x 12.4 keV photons reported in Table 6 and the delta of 3.9 x 12.4 keV photons between the last point in HG and first point in the MG reported in Table 19.

Table 6: Voltage steps used for the sensor backside injection

(Start : Δ : Stop) [mV]	Δ [x 12.4 keV ph.]
(25 : 25 : 1000)	1.95
(1025 : 100 : 8425)	7.8

Concerning the granularity, the time-to-calibration and the possibility to synchronize it with the detector, all the considerations made for the current source are valid for this source. Moreover, concerning the radiation tolerance, the uniformity of injection and the independence from the ASIC, all the considerations are the same as for the LED light. The source itself (backside pulsing amplifier) can be independently characterized, especially in terms of linearity. This source makes use of the sensor capacitance as injection capacitance, which is highly radiation tolerant. The timings are very well defined and the measurement does not require the integration time to be changed, avoiding the more complex offset correction already mentioned for the current source and the LED light. This source is also easily available at the experimental site.

The DR that can be probed depends on the maximum voltage step that can be applied to the backside of the sensor and the coupling capacitance between anode and backside. For this detector this is around 8 fF. With the designed amplifier, the maximum charge injection achievable (35 V voltage step) corresponds to $\sim$ 700 x 12.4 keV photons allowing to explore the dynamic range only up to the MG. As a consequence this technique works better for detectors that have a higher coupling between anode and backside such as strip detectors.

10.1. Calibration

Unlike the last two sources described the scan parameter is not the integration time but the pulse amplitude. In this case, the calibration follows the one described in Sec. 8.1 from point 2) on, given that the x-axis is now in V, as is the offset to correct the x-axis. In this case, the offset is (6.440 ± 0.006) mV. The calibrated output curve is shown in Fig. 21. The first point after the first gain switching, indicated with the red arrow causes a non-monotonicity of the output curve in this point. In case the settling time is well defined and is above (or equal to) 125 ns, this happens when the charge injection cause the output voltage of the preamplifier to be very close to the switching point and therefore a gain switching can happen because of the noise, at a random time close to the disconnection of the storage cell. This behavior, in this ASIC, cannot be completely eliminated and can be seen only with a calibration source that has a granularity that allows to finely sample the DR.

The fit results are reported in Table 7 (fit limits (80,500) x 12.4 keV photons). In Fig. 22 the remainders of the fit are shown. As can be seen, there is no

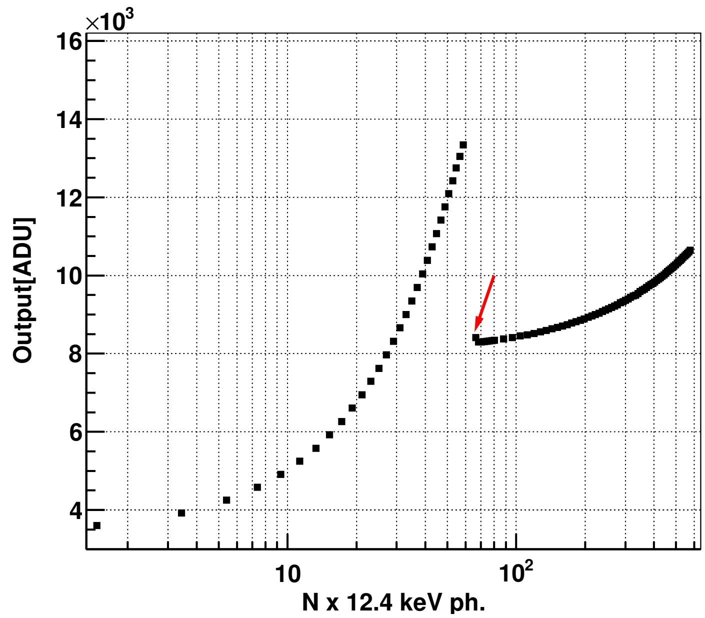

Figure 21: Calibrated output obtained pulsing the backside of the sensor. The high gain and half of the medium gain region can be seen. The red arrow indicate a point after the gain switching that causes a non-monotonicity of the curve. This point is visible thanks to the fine granularity of this source.

bending of the output curve, i.e. the curve is very linear. This fact leads to two conclusions. First, the gain and offset obtained in the MG with this method are most probably more reliable. Second, since the linearity of the backside pulsing amplifier was tested separately and resulted to be better than 0.5% the bending observed in the MG region (in the range up 500 x 12.4 keV photons) for the other two sources previously shown can either be caused by the source itself or by a variation of internal references (currents or voltages) of the ASIC with the integration time.

Table 7: Gains and offsets in the MG for backside pulsing

Gain $\frac{[ADU]}{[keV]}$	Offset $[ADU]$
0.3739 ± 0.0003	7970 ± 1

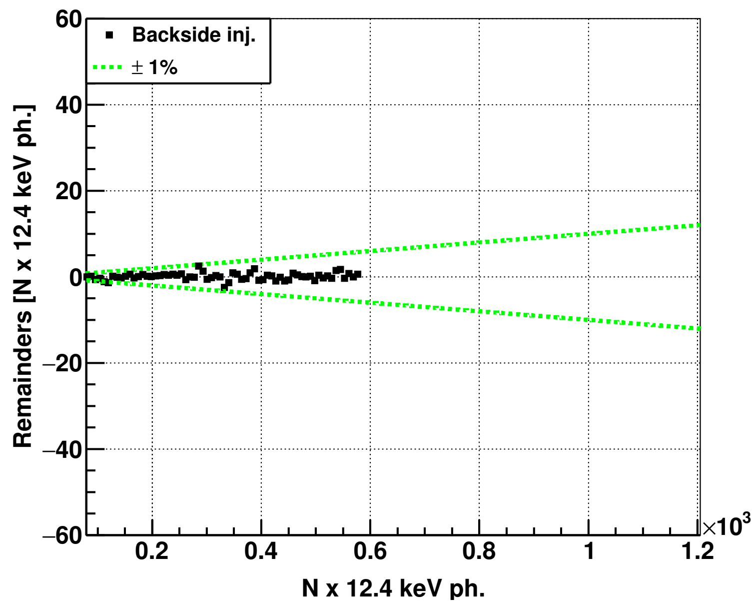

Figure 22: Remainders (in 12.4 keV ph.) of the linear fit of the backside pulse data in the MG region, in the fitted range. In green the $\pm 1\%$.

11. DR scan with an IR pulsed laser

The DR has been tested on a single pixel level with an IR pulsed laser (wavelength $\lambda = 1030$ nm, absorption length $L_{abs} \approx 341$ μm). The wavelength of the laser has been chosen such that the absorption length is similar to that of X-ray photons (at the target energy of 12.4 keV) so that the real experimental condition at the EuXFEL could be reproduced in the lab.

In our measurements, the ASIC test setup sends a trigger signal to a delay generator which in turn triggers the laser. In this way, an accurate delay scan (as the one shown in [2]) of the integration window can be performed and timings precisely defined. Moreover, the integration time is fixed avoiding any variation of the offset as a function of it.

The laser beam has been focused on a single pixel (beam spot < 10 μm). The Aluminum was removed from the backside. The intensity of the laser has been manually set to the maximum DR of the pixel and the beam has been attenuated with a set of independently calibrated filters. The calibration of the filters has been done by measuring the current of a diode from a standard sensor wafer. The sweep parameter, in this case, is the filter intensity (attenuation). Since in our setup there are only 60 possible combinations of filters, to make a fine scan of the DR, the intensity of the laser has been modified (lowered) manually 6 times and every single measurement has been calibrated for a total of 360 measurement points.

Since the sampling of the DR is not uniform, a table to show the granularity of this source is not given as for the previous sources. Instead the last and first points before and after each gain switching (critical areas of the DR for this detector) are given. These numbers can be found also in Table 19. The granularity is given by the number of filters and by the number of measurements acquired at different laser intensities. For this detector a good sampling of the DR is achieved when the region after the gain switching is finely sampled in order to be able to see a deviation from the linear behavior or even a non-monotonicity. This is normally achieved for a number of measurements above 5 (or number of points above 300).

For our setup, an independent calibration of the filters is needed and its reliability over time has to be proven (different filter degradation, dust, etc.).

11.1. Calibration

In this case, the x-axis is in arbitrary units that are proportional to the current measured by the photodiode used for the calibration of the filters. Every single curve (6 in total) with 60 points has been fitted and the correction factor has been computed. The calibration then follows, as the backside pulsing, the points 2) to 5) in Sec. 8.1.

The calibrated output curve is shown in Fig. 23. The first point after the first gain switching, indicated with the red arrow causes a non-monotonicity of the output curve in this point. As reported in Table 19 this point is at higher number of photons with respect to the first point sampled in the MG by the sensor backside pulsing. The reason for this behavior is, most probably, the ionization profile and the charge transport in the sensor. The delay scan shows (see [2]) a rather smooth falling edge. This can lead to an error in the evaluation of the settling time of few nanoseconds producing this non-monotonic point (or few points) on the output curve.

The fit results for the MG and LG are reported in Table 8. The fit ranges of the linear fit are (80,1200) x 12.4 keV ph. in MG and (1400,7000) x 12.4 keV ph. in LG. In Fig. 24 and 25 the remainders of the linear fit in the MG and LG regions are shown. As can be seen, the linearity is better in the MG when compared to the current source and LED illumination and in the LG a bending of the curve is visible. This might be due to a longer charge collection time at high intensity that can be avoided with sensor bias higher than the 240 V used for all the measurements. The main difference with respect to the other sources consists in the gain value in the LG region. This difference arises either from the different setup used for the filter calibration with respect to our setup, or from the degradation of the filters with time, affecting the long term stability of their calibration.

Table 8: Gains and offsets for IR laser

Gain region	Gain $\frac{[ADU]}{[keV]}$	Offset $[ADU]$
MG	0.3743 ± 0.0004	7951.5 ± 0.1
LG	0.08954 ± 0.0003	8153 ± 1

12. DR scan with monoenergetic protons

In this contribution, we investigated the possibility to use a pulsed monoenergetic proton beam as a diagnostic tool to explore the DR and compare the calibration curve with the other sources. Similar to photons in the HG range, protons serve as an absolute reference for the MG and LG ranges. We take advantage of performing tests with protons in air with a technique developed in [18] featuring a well defined proton extraction window and proton energy loss

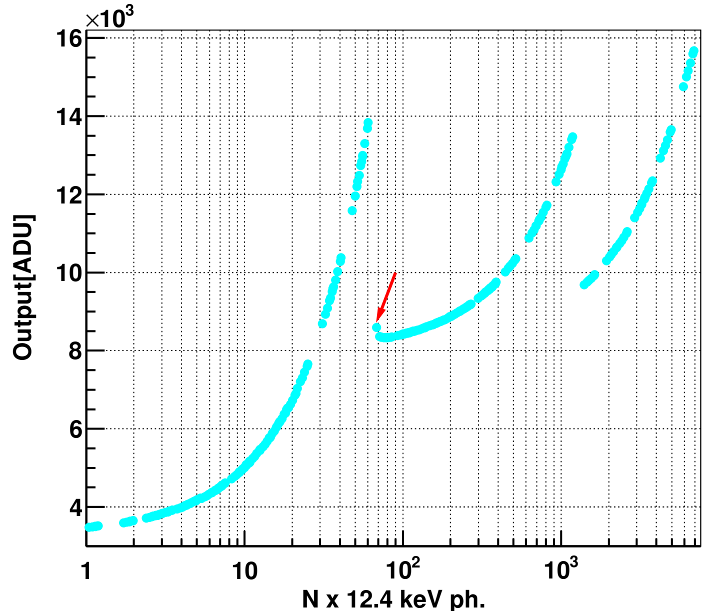

Figure 23: DR scan obtained irradiating the pixel with an IR pulsed laser (wavelength $\lambda = 1030$ nm) and moderating the beam with a set of independently calibrated filters. Every point is the average of 1000 measurements. There are a total of 360 measurement points.

in air as a function of distance. The pulsed proton beam comes from the DEFEL beamline [19] of the TANDETRON accelerator of LABeC (Laboratorio di Tecniche Nucleari per i Beni Culturali), located in Sesto Fiorentino (FI), Italy. Due to its fast electrostatic chopper, a pulsed proton beam can be created out of the continuous one coming from the accelerator. This is particularly important in case of the AGIPD detector since it can be synchronized with the proton beam and the timings, e.g. the settling time, can be very well defined (a trigger is provided from the chopper). Moreover, the minimum beam spot size has been measured [20] around (60 x 40) μm r.m.s. so it can be focused on a single pixel. The proton energy can be tuned in the range 1 MeV to 6 MeV (penetration depth in Silicon from 16 μm to 295 μm). Energies lower than 1 MeV can be obtained by tuning the distance between the detector and the exit window of the proton pipe, i.e. the length of the proton flight path in air.

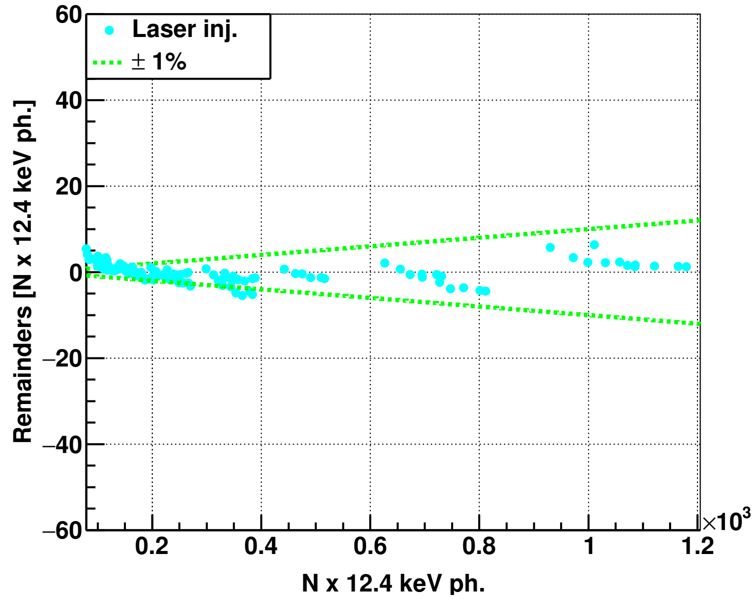

Figure 24: Remainders (in 12.4 keV ph.) of the linear fit of the laser data in the MG region, in the fitted range. In green the $\pm 1\%$.

For this work, two target proton energies were chosen: 1 MeV and 3 MeV. The proton energy is very stable over the measurement time. In Fig. 26 a SRIM (Stopping and Range of Ions in Matter) simulation showing the ionization profile of 1 MeV protons in silicon for 10 different air thicknesses is shown, while Fig. 27 shows the energy loss of 1 MeV protons as a function of the air thickness. Every single point of the curve of Fig. 27 is obtained by subtracting from 1 MeV the integral of the curve of Fig. 26 for the corresponding air thickness. For air thicknesses from 0 mm up to 10 mm the energy loss can be well described with a linear relation and from the linear fit (in red) the energy loss has been estimated to be 2914.74 $[\frac{eV}{100\ \mu m}]$.

In Table 9 the energy collected (in keV) as a function of the air thickness (in mm) is reported. The attenuation for 1 MeV protons is very effective, reducing the energy released in the sensor by up to 30% when increasing the flight path from 0 mm to 10 mm of air. Moreover, since the gain switching point is around

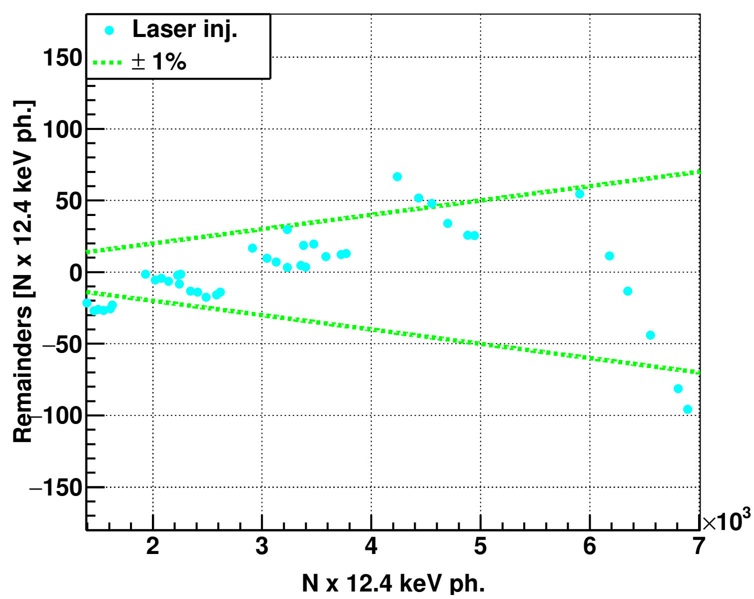

Figure 25: Remainders (in 12.4 keV ph.) of the linear fit of the laser data in the LG region, in the fitted range. In green the ±1%.

800 keV, it is possible to have a measurement point in HG with an air thickness above 7 mm.

The energy attenuation with air is less effective (in %) for 3 MeV protons, therefore, the decision was to use the 1 MeV protons and moderate the beam with different air thicknesses to finely sample the first part of the MG and to have a measurement point in HG and the 3 MeV protons to explore up to the LG by using the proton multiplicity. The multiplicity itself also guarantees the linearity of the source. To scan the DR, one can tune the average amount of protons per bunch down to an average value well below one and up to several tens. The 1 MeV proton energy has been further reduced by interposing 3 mm, 5 mm and 10 mm of air between the detector and the exit window, while for the 3 MeV protons the distance between the pipe and the sensor was 5 mm. The proton energies have been independently calibrated with an ^{241}Am alpha source (5.486 MeV) and are reported in Table 10 together with an error that

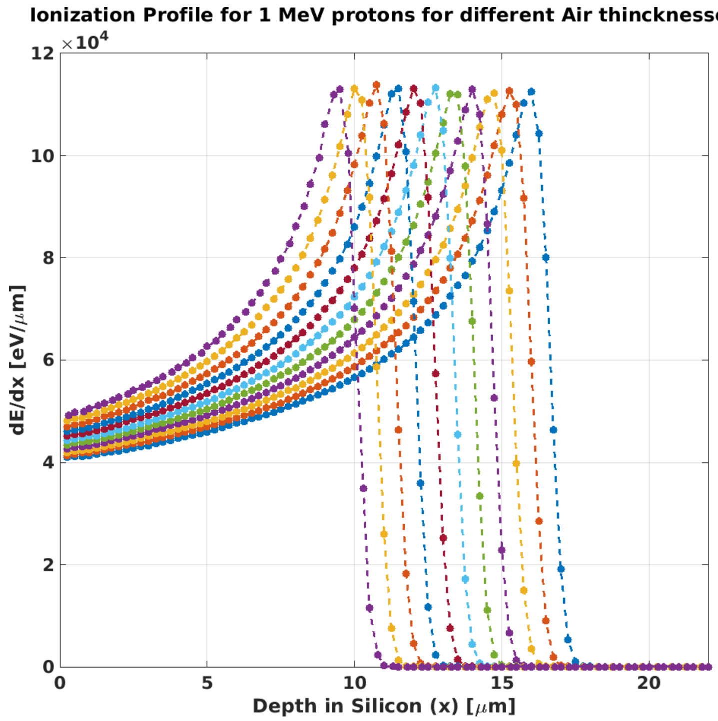

Figure 26: Ionization profile in Si for 1 MeV protons for 10 different air thicknesses (reported in Table 9). The right most curve is relative to 0 mm of air and the left most to 10 mm of air.

is estimated in the order of ± 1%. The difference with the simulated values reported in Table 9 is due to the initial proton energy that is slightly different from the nominal values.

As for the IR laser, the sampling of the DR is not uniform therefore it is difficult to define the granularity. An information about the granularity is given in Table 10, assuming that whenever more than a single proton impinge on the pixel cluster, the energy released is a multiple of that given in the third column. As for the laser, useful information are the last and first points before and after each gain switching. As for the other sources these numbers can be found in Table 19. Although by modulating the proton energy with different air thicknesses the granularity of this source can be significantly improved with respect to the case of the measurement performed in vacuum and therefore with

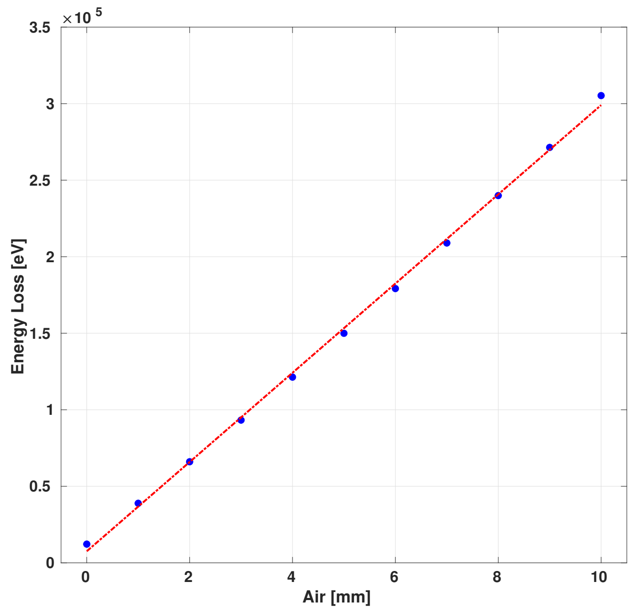

Figure 27: Energy loss as a function of mm of air for 1 MeV protons. The points are obtained by subtracting the area of the curves in Fig. 26 from the nominal energy of 1 MeV. From a linear fit the energy loss is 2914.74 $[\frac{eV}{100\ \mu m}]$

.

a fixed energy, it is still worse than the other calibration sources presented in this contribution.

The temperature inside the experimental chamber has been monitored during the entire duration of the beamtime, and was found to be stable within a band of 5 °C. This, however had a negligible effect on the offset which was regularly measured during the beamtime.

12.1. Gain stability with gain switching

A first and very important result obtained using this source is the proof that there is no influence of the gain switching on the gain value. For this measurement, the proton beam has been focused on a single pixel and the data were acquired in normal operation mode (gain switching active) and with the

Table 9: Energy collected vs mm of air for 1 MeV protons

Air thickness [mm]	Energy collected [keV]
0	987.78
1	961.1
2	933.96
3	906.75
4	878.67
5	850.04
6	820.81
7	791.04
8	760.07
9	728.6
10	694.73

Table 10: Proton energies from calibration with ^{241}Am

Nom. En. [MeV]	Air [mm]	Cal. En. [MeV]	Error [MeV]
1	3	0.917	$\pm$ 0.009
1	5	0.857	$\pm$ 0.009
1	10	0.718	$\pm$ 0.007
3	5	3.06	$\pm$ 0.03

gain fixed to the medium value. The nominal energy of the protons was 1 MeV and 4 proton peaks were fitted in both cases and the gain has been extracted by the linear fit shown in Fig. 28. The measured gain, within the error of the measurement, is the same whether the gain switching is active or not. It has to be noted that for this measurement an absolute calibration of the proton energy is not required.

12.2. Calibration

The calibration in the case of proton irradiation is a bit different since for high level of charge injection (several 1 MeV or few to several 3 MeV protons) the charge is not fully collected by the central pixel but also by the neighbors.

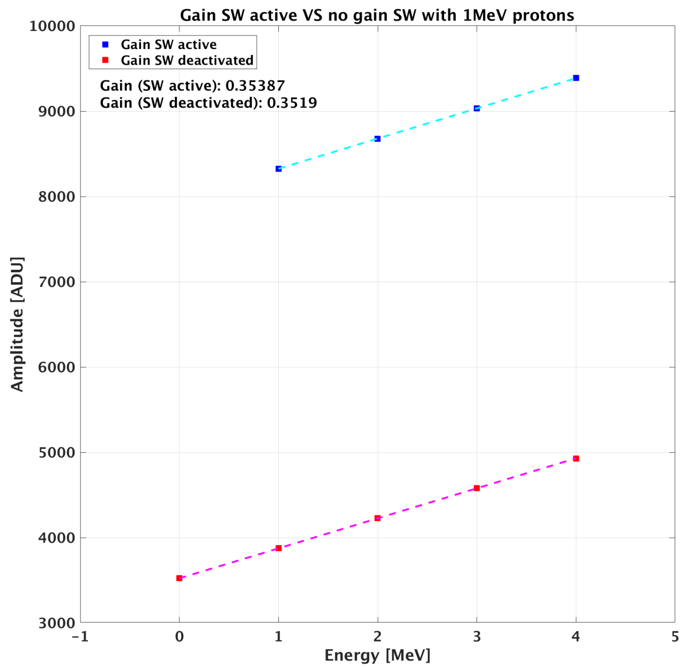

Figure 28: Comparison between the gain evaluated in the MG region with 1 MeV protons with gain switching active (blue curve) and gain switching deactivated (red curve). The gain has been evaluated in the first case by fitting four 1 MeV proton peaks and in the second case by fitting also the noise peak. The offset between the two curves is caused by the absence of charge injection from the gain switches when operating in fixed gain mode.

This is due to protons impinging close to the CE pixel edge or in one of the neighboring pixels. For the calibration of this source the whole pixel cluster of Fig. 6 is considered and for every frame (triggered by the DEFEL trigger) the signal in the neighboring pixels will be summed to the CE one in the following way:

1. If all the 9 pixels are in HG: the frame is empty and discarded;
2. CE pixel in LG, in this case:
    - If a single neighboring pixel is in LG the CE pixel did not integrate the major part of the signal so the frame is discarded;

- Check the neighboring pixels that are in the HG and sum their amplitude after correction of the gain with respect to CE as:

$$A_{HL} = \sum_{pix \,\in\, HG} [A(pix) - O_{HG}(pix)] \cdot gr_{HG}(pix) \qquad (22)$$

- Check the neighboring pixels that are in the MG and sum their amplitude after correction of the gain with respect to CE as:

$$A_{ML} = \sum_{pix \,\in\, MG} [A(pix) - O_{MG}(pix)] \cdot gr_{MG}(pix) \qquad (23)$$

- The amplitudes are then summed to the amplitude in LG for the central pixel as:

$$A_{LG,tot} = A_{LG} + A_{ML} \cdot gr_{LM} + A_{HL} \cdot gr_{MH} \cdot gr_{LM} \qquad (24)$$

3. CE pixel in MG, in this case:
   - If even a single neighboring pixel is in MG the CE pixel does not have the major part of the signal so the frame is discarded;
   - If all the neighboring pixels are in the HG their amplitude is summed after correction of the gain with respect to CE as:

$$A_{HM} = \sum_{pix \,\in\, HG} [A(pix) - O_{HG}(pix)] \cdot gr_{HG}(pix) \qquad (25)$$

   - The amplitudes are then summed to the amplitude in MG for the central pixel as:

$$A_{MG,tot} = A_{MG} + A_{HM} \cdot gr_{MH} \qquad (26)$$

All the parameters introduced in the equations (22), (23), (24), (25) and (26) together with their definition and how they are evaluated can be found in Table 11. The gain ratio gr_{HG} has been determined using fluorescence photons, gr_{MG} and gr_{MH} using backside pulsing and gr_{LM} using the current source. In the case of 1 MeV protons, for 3 and 5 mm of air thicknesses, the same procedure described in 3. is applied. For 10 mm of air thickness, the procedure for the

Table 11: Meaning of the parameters

Par. name	Definition	Evaluation source
A_{HL}	Temporary amplitude referred to the CE pixel in HG to be summed in the LG	See (22)
A_{ML}	Temporary amplitude referred to the CE pixel in MG to be summed in the LG	See (23)
A_{HM}	Temporary amplitude referred to the CE pixel in HG to be summed in the MG	See (25)
$A_{LG.tot}$	Total amplitude of the CE pixel in LG	See (24)
$A_{MG.tot}$	Total amplitude of the CE pixel in MG	See (26)
$A(pix)$	Analog output of the considered pixel	Direct measurement
A_{MG}	Analog output of the CE pixel in MG	Direct measurement
A_{LG}	Analog output of the CE pixel in LG	Direct measurement
$O_{HG}(pix)$	Offset of the considered pixel in HG	Direct measurement
$O_{MG}(pix)$	Offset of the considered pixel in MG	Backside pulsing
$gr_{HG}(pix)$	Gain ratio in HG between the considered pixel and CE	Fluorescence photons
$gr_{MG}(pix)$	Gain ratio in MG between the considered pixel and CE	Backside pulsing
gr_{MH}	Gain ratio between MG and HG for the CE pixel	Backside pulsing
gr_{LM}	Gain ratio between LG and MG for the CE pixel	Current source

MG is the same as for 3 and 5 mm of air while for the HG all the amplitudes of the neighboring pixels are summed to the CE by using the $gr_{HG}(pix)$.

After treating the data in the way just described a Gaussian fit of the proton peaks is performed. In Fig. 29 5 and in Fig. 30 10 proton peaks (of 3 MeV nominal energy) are visible in MG and LG for the CE pixel respectively. The number of protons impinging the detector follows the Poisson statistics and the reason why this does not seem to be the case for the two distributions in Fig. 29

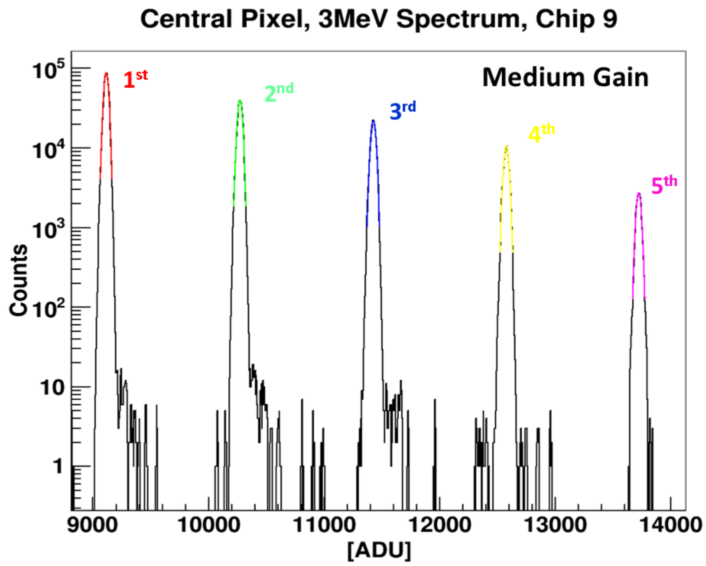

Figure 29: Proton peaks in MG for 3 MeV protons after summing the neighboring pixels to the central one. 5 proton peaks are visible and fitted.

and 30 is because of the applied filtering treatment of the data described above. After all the peaks have been fitted, for all the proton energies and all the air thicknesses, the calibration data reported in Table 10 are applied. The result for all the three gain stages is shown in Fig. 31. In Fig. 32 and 33 the remainders of the linear fit in MG and LG are shown. As for the other calibration sources that are working with fixed integration time no bending of the output curve is visible either in MG or LG (the probed part). The results of the linear fit can be found in Table 12.

Table 12: Gains and offsets for proton irradiation

Gain region	Gain $\frac{[ADU]}{[keV]}$	Offset $[ADU]$
MG	0.380 ± 0.002	7982 ± 6
LG	0.084 ± 0.002	8148 ± 66

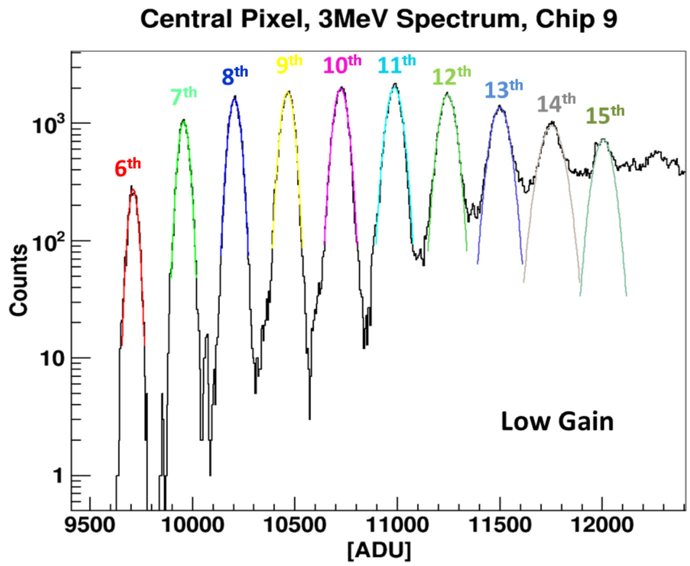

Figure 30: Proton peaks in LG for 3 MeV protons after summing the neighboring pixels to the central one. 10 proton peaks are visible and fitted.

13. Offsets with triggered gain switching

The easiest way to obtain the offset values in MG and LG is by triggering the gain switching during the integration window without any signal (charge integrated on the feedback capacitor). This is by definition the offset since it is the output value in a gain region (taking into account the charge injection due to the gain switching) without any signal charge integrated (see equation (3) and (4)). In the case of the AGIPD ASIC, this can be done by programming the gain switching to happen during the integration window (marked red in Fig. 3) using the control periphery. This method has the big advantage that the offsets can be obtained quickly with only 2 measurement points to be acquired instead of acquiring a full DR curve and performing a data analysis. This advantage is particularly relevant, because it allows acquiring the offsets in MG and LG for the entire system (1 Mpixel with 352 storage cells per pixel) even during an experiment, allowing to immediately check the stability of the system and have correction data at different times during the experiment to be used in the

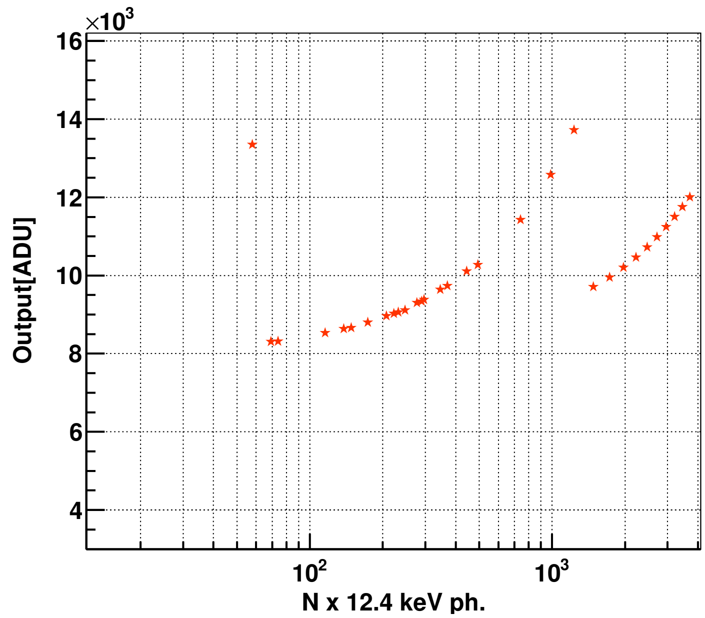

Figure 31: DR scan obtained by irradiating with monoenergetic protons of different energies and moderating the beam with different air thicknesses.

post-processing analysis. The offsets obtained with this method are reported in Table 13.

Table 13: Offset by triggering the gain switching without signal

Gain region	Offset $[ADU]$
MG	8209.7 ± 0.2
LG	8503.4 ± 0.2

The main disadvantage of this method is that the gain switching happens with the preamplifier feedback capacitor in a different state (no charge integrated, $V_{Cf} = 0$ V) with respect to the real situation ($V_{Cf} =$ few hundreds of mV). Since the MG and LG feedback capacitors are added in the feedback loop of the preamplifier by means of a transistor and the offsets with respect to the HG are due to the charge injection of these two switches, there might be a different charge redistribution caused by the different potential situation at

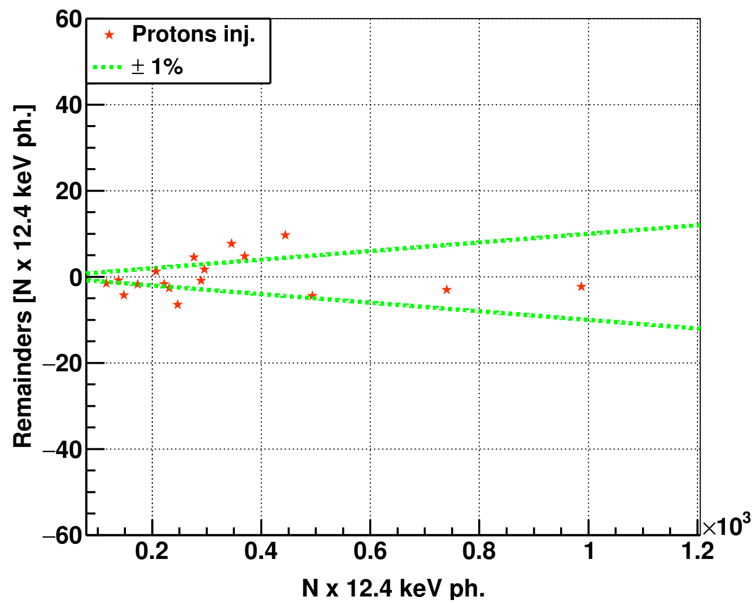

Figure 32: Remainders (in 12.4 keV ph.) of the linear fit of the proton irradiation data in the MG region, in the fitted range. The green lines indicate a non-linearity of $\pm 1\%$.

the two terminals (source and drain) of the transistors causing slightly different offsets. This is at the moment not supported by any data or simulation. To carefully study what is happening under these circumstances one should perform detailed simulations of the charge injection under different conditions and crosscheck with experimental data. This has not been done and is beyond the scope of this contribution.

14. Comparison of results

In Table 14 the average gain (Av. gain) obtained with the different methods is reported together with the minimum and the maximum values and the percentage variation for the MG and LG. In Table 15 the average offsets (Av. off) in [ADU] for the MG and the LG regions are reported together with the minimum and the maximum values and the variation with respect to the average

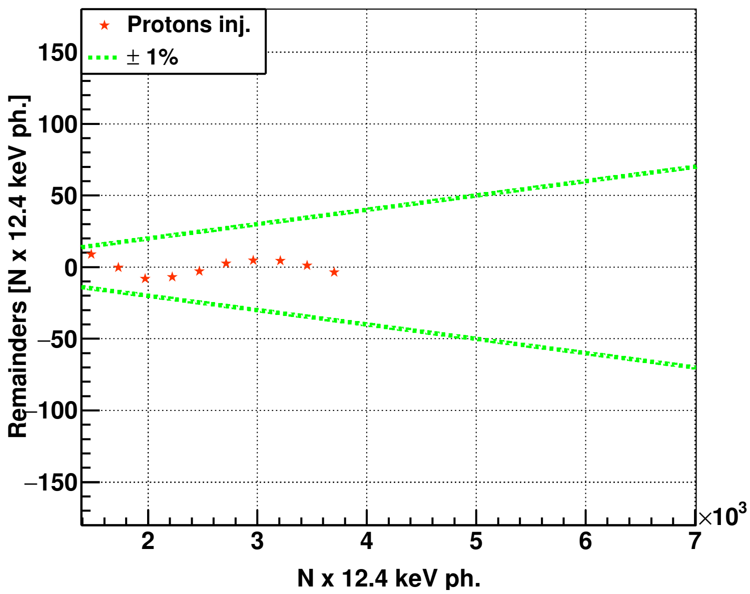

Figure 33: Remainders (in 12.4 keV ph.) of the linear fit of the proton irradiation data in the LG region, in the fitted range. The green lines indicate a non-linearity of ±1%.

850 (Δ). In Table 16 the offset variations (min and max) are reported in terms of
851 number of 12.4 keV photons by taking the (Δ) of Table 15 and dividing it by
852 the average gain reported in Table 14.

Table 14: Gain variation (max/min) for different calibration methods

Gain reg.	Av. gain $[\frac{ADU}{keV}]$	min $[\frac{ADU}{keV}]$(%)	max $[\frac{ADU}{keV}]$(%)
MG	0.3733	0.3614 (-3%)	0.3825 (+2.5%)
LG	0.08185	0.0756 (-7.6%)	0.08954 (+9.4%)

Table 15: Offset variation (max/min) for different calibration methods in [ADU]

Gain reg.	Av. off $[ADU]$	min(Δ) $[ADU]$	max(Δ) $[ADU]$
MG	8042	7951(-91)	8209 (+167)
LG	8332	8148 (-184)	8574 (+242)

853 Table 17 summarizes the gains in MG and LG, obtained with the different

Table 16: Offset variation (max/min) for different calibration methods in [12.4 keV $ph.$]

Gain reg.	min(Δ) [12.4 keV $ph.$]	max(Δ) [12.4 keV $ph.$]
MG	-19.7	+36
LG	-181.3	+238.4

calibration sources and the relative variation with respect to the average values (also reported). Table 18 summarizes the offsets in MG and LG, obtained with the different calibration sources and the absolute variation in number of 12.4 keV photons calculated as for the Table 16.

In Table 19 the information about the linearity and granularity are reported for the different calibration sources used. The linearity (2^{nd} and 3^{rd} column) has been reported in terms of maximum positive and negative deviation from the linear fit in the MG and LG region in the fitted range. The deviations from the linear fit are given in terms of number of 12.4 keV photons and are obtained by converting the deviations from the linear fit from [ADU] using the gain evaluated for the corresponding source in $\frac{[ADU]}{[keV]}$. Because for this ASIC the two most critical areas of the DR are the ones directly after the gain switching, the granularity has been reported in the (opinion of the authors) most synthetic and meaningful way for this detector that is in terms of the last and first points tested for each gain region (4^{th} and 5^{th} column).

All the sources used, with their advantages, disadvantages and the scanning parameters are summarized in Table 20. The calibrated curves for the entire DR are shown in Fig. 34. For completeness, in Table 20 the DR scan using the internal (in-pixel) pulsed capacitor is mentioned even if it has not been shown in this contribution (see [8]).

15. Summary

In this contribution, two main subjects have been presented. First, the problem of the calibration of a fast, high DR, charge integrating detector with dynamic gain switching. Second, the comparison between different calibration

Table 17: Summary of all the gains and offsets obtained in MG and LG for all the sources. Average values are also reported. In brackets the relative deviations with respect to the average.

Calibration Method	$Gain_{\mathrm{MG}}(\Delta)\ \frac{[ADU]}{[keV]}(\%)$	$Gain_{\mathrm{LG}}(\Delta)\ \frac{[ADU]}{[keV]}(\%)$
Average values	0.3733	0.08185
Int. current source (64 pix)	0.3674 (-1.6 %)	0.07661 (-6.4 %)
Int. current source (4096 pix)	0.3825 (+2.5 %)	0.0756 (-7.6 %)
LED light	0.3614 (-3.2 %)	0.0835 (-2 %)
Sensor Backside Pulsing	0.3739 (+0.2 %)	Only MG
IR pulsed laser	0.3743 (+0.3 %)	0.08954 (+9.4 %)
Pulsed monoen. proton beam	0.38 (+1.8 %)	0.084 (+2.6 %)
Gain sw. externally triggered	Only offset	Only offset

Table 18: Summary of all the offsets obtained in MG and LG for all the sources. Average values are also reported.

Calibration Method	$Off_{\mathrm{MG}}(\Delta)$ [ADU](12.4 keV $ph.$)	$Off_{\mathrm{LG}}(\Delta)$ [ADU](12.4 keV $ph.$)
Average values	8042	8332
Int. current source (64 pix)	8071.6 (+6.8)	8462 (+128.1)
Int. current source (4096 pix)	8110.8 (+14.9)	8574 (+238.4)
LED light	7996 (-9.9)	8153 (-176.3)
Sensor Backside Pulsing	7970 (-15.6)	Only MG
IR pulsed laser	7951.5 (-19.7)	8153 (-176.3)
Pulsed monoen. proton beam	7982 (-13)	8148 (-181.3)
Gain sw. externally triggered	8210 (+36)	8503 (+168.5)

methods and sources, highlighting the advantages and disadvantages of each one.

Due to its features, AGIPD represents a perfect calibration test case. On one hand to investigate the different calibration sources and their capabilities, on the other for the need of the development of a mathematical model for the

Table 19: Deviations from linear fit and last and first points tested for each gain region. All numbers are in $N\ x\ 12.4\ keV\ ph$.

Calibration Method	Max pos. dev. MG\LG	Max neg. dev. MG\LG	Last HG\First MG\Δ	Last MG\First LG\Δ
Int. current source (64 pix)	19.0 @x = 438.9 21.4 @x = 3628	-21.2 @x = 1194.7 -36.8 @x = 6773	64.01\67.03\3.02	1270.3\1345.9\75.6
Int. current source (4096 pix)	15.1 @x = 442.9 26.2 @x = 4395	-19.1 @x = 1129.6 -41.6 @x = 6837	61.40\64.45\3.05	1205.9\1282.2\76.3
LED light	3.9 @x = 451.6 14.2 @x = 6911	-12.1 @x = 119.5 -28.4 @x = 5582	61.36\63.03\1.67	1240.3\1281.8\41.5
Sensor Backside Pulsing	2.5 @x = 285.1 Only MG	-2.5 @x = 332.4 Only MG	60.56\64.46\3.9	584\Only MG
IR pulsed laser	6.4 @x = 1010.9 66.7 @x = 4238	-5.42 @x = 365.1 -95.7 @x = 6895	60.43\68.08\7.65	1179.6\1396.7\217.1
Pulsed monoen. proton beam	9.7 @x = 443.8 9 @x = 1481	-6.5 @x = 246.8 -8.1 @x = 1974	57.87\69.01\11.14	1233.9\1480.6\246.7

data treatment. To perform its calibration, a basic mathematical model has been developed and shown in Sec. 3. A minimum of 6 parameters (3 gains and 3 offsets) for every pixel plus 2 per storage cells are needed in the ideal case. This model is particularly suitable to keep the total number of parameters to calibrate the final system to a manageable level by assuming a simple linear model for the three gain regions. This basic model has then been modified to take into account the coupling between the pixels explained in Sec. 5.

As can be deduced from the results and the discussion of this paper, often a calibration suite is not represented by a single source but by few sources that, by exploiting their different advantages can be used to calibrate the detector and mutually mitigate the weaknesses of single sources. The best way to calibrate this detector is to use the backside pulsing (best linearity) up to the maximum coverable injection level and then use the current source to cover the remaining part of the DR. Due to practical reasons this was not implemented in the final system and, therefore, only the on-chip sources have been used.

The spread of the offset and gain with respect to the average value obtained by using all the sources presented, is partly due to the difference between the

Table 20: Comparison between different calibration sources. Advantages and disadvantages

Calibration Method	Parameters	Advantages	Disadvantages
Fluorescence photons	• Energy • # photon peaks	• Absolute calibration in HG	• Limited DR
Internal current source	• Integration time	• Programmable • Flexible and easy to use • Well defined timings	• Require power from the ASIC • Potential non linearity at the gain switching • Sensitive to offset drift with the integration time • Sensitive to radiation damage
LED light	• Integration time	• Independent from the ASIC • Uniform illumination • Radiation hard	• Removal of Al from backside • Timings not well defined • Sensitive to offset drift with the integration time
Internal pulsed capacitor (See [8])	• Pulse height (PH)	• Programmable • Flexible and easy to use • Well defined timings • Measure with fixed integration time • Radiation tolerant	• Parameters like PH, risetime etc. might vary a lot over the ASIC • Limited DR due to limited PH • Bad Linearity
Sensor backside pulsing	• Pulse height (PH)	• Independent from the ASIC • Uniform injection • The parameters of the pulse (like risetime) can be adjusted • Well defined timings • Measure with fixed integration time • Best measured linearity • Radiation hard (source) + radiation tolerant (sensor capacitance)	• Limited DR due to limited PH (35 V for the actual setup) • All the pixels pulsed at once
IR pulsed laser	• Laser intensity • Calibrated filters	• Independent from the ASIC • Simulate charge injection as in the real experimental case • Well defined timings • Measure with fixed integration time • Radiation hard (source)	• Scan only few pixels • Potential drift of the laser pulse height with time • Require calibration of the filters • Not available in-situ
Pulsed monoenergetic proton beam	• Proton energy • # Protons	• Independent from the ASIC • Simulate charge injection as in the real experimental case • Well defined timings • Measure with fixed integration time • Radiation hard (source)	• Scan only few pixels • Not available in-situ

sources but mostly from the shortcomings/features of the detector under test (AGIPD) and/or the parameter used to sweep the DR. However, it has been demonstrated that with a careful data treatment that takes into account the

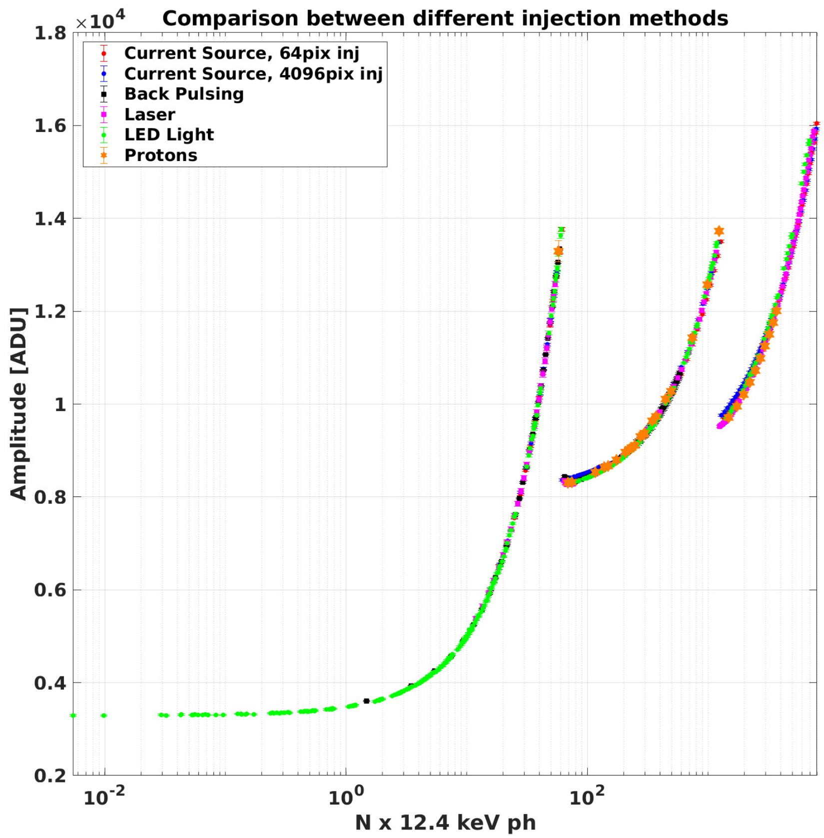

Figure 34: DR scan obtained with all the sources presented and discussed in this contribution.

main shortcomings (i.e. coupling and offset variation as a function of the integration time in this paper) it is possible to obtain comparable results with a limited variation across the different methods/sources. This fact has been numerically quantified and summarized in Table 19 and can be visually seen in Fig. 34. Moreover, this variation can or might not be critical depending on the application. Due to these reasons, the authors would like to point out that what was presented in this contribution represents the first step or the initial calibration of the detector. The calibration results obtained by using any of the sources presented and/or any mathematical model (depending on the detector) have to be constantly checked against real experimental data. The collaboration and communication between the detector development groups and the user/scientific community using the detector is therefore of fundamental importance.

References

[1] X. Shi et al., Challenges in chip design for the AGIPD detector, Nucl. Instr. Meth. A, 624 (2) (2010) 387-391.

[2] D. Mezza et al., Characterization of AGIPD1.0: the full scale chip, Nucl. Instr. Meth. A, 838 (2016) 39-46.

[3] M. Altarelli et al., European xfel technical design report, ISBN 978-3-935702-17-1, 2006.

[4] A. Castoldi et al., Calibration sources and techniques for large format X-ray imagers at XFEL, in: IEEE Nuclear Science Symposium and Medical Imaging Conference Record, 2016, pp. 1-3.

[5] H. Graafsma, Requirements for and development of 2 dimensional X-ray detectors for the European X-ray Free Electron Laser in Hamburg, J. Instrum. 4 (2009) P12011.

[6] X. Shi et al., A low noise high dynamic range analog front-end ASIC for the AGIPD XFEL detector, in: Proc. 19th IEEE Int. Conf. Electronics, Circuits and Systems, ICECS, 2012, pp. 933-936.

[7] D. Mezza et al., Characterization of the AGIPD1.1 readout chip and improvements with respect to AGIPD1.0, Nucl. Instr. Meth. A, 945 (2019) 162606.

[8] A. Allahgholi et al, The Adaptive Gain Integrating Pixel Detector at the European XFEL, J. Synchrotron Rad. 26 (2019) 74–82.

[9] J. Zhang et al., Investigation of X-ray induced radiation damage at the Si-SiO2 interface of silicon sensors for the European XFEL, http://arxiv.org/abs/1210.0427.

[10] J. Zhang et al., Study of radiation damage induced by 12 keV X-rays in MOS structures built on high-resistivity n-type silicon, J. Synchrotron Rad. 19 (2012) 340–346.

[11] J. Zhang et al., Towards Gotthard-II: development of a silicon microstrip detector for the European X-ray Free-Electron Laser, J. Instrum. 13 (2018) P01025.

[12] J.B.A. England et al., Capacitative charge division read-out with a silicon strip detector, Nucl. Instr. Meth. A, 185 (1981) 43-47.

[13] W. Dabrowski et al., Charge division in silicon strip detectors with a large strip pitch, Nucl. Instr. Meth. A, 349 (1994) 424-430.

[14] M. Krammer and H. Pernegger, Signal collection and position reconstruction of silicon strip detectors with 200 μm readout pitch, Nucl. Instrum. Meth. A, 397 (1997) 232-242.

[15] U. Trunk for the AGIPD collaboration, The AGIPD 1.0 ASIC manual.

[16] D. Mezza et al., New calibration circuitry and concept for AGIPD, J. Instrum. 11 (2016) C11019.

[17] S. Redford et al., First full dynamic range calibration of the JUNGFRAU photon detector, J. Instrum. 13 (2018) C01027.

[18] A. Castoldi et al., Validation of proton tests in air for detector calibration over a wide range of charge injection levels, in: IEEE Nuclear Science Symposium and Medical Imaging Conference Record, 2015, pp. 1-3.

[19] F. A. Mirto et al.,The pulsed beam facility at the Tandetron accelerator in Florence, Nucl. Instrum. Meth. B, 266 (2008) 2113-2116.

[20] A. Castoldi et al., Upgrade of the DEFEL proton beam line for detector response mapping, in: IEEE Nuclear Science Symposium and Medical Imaging Conference Record, 2013, pp. 1-5.